JHEP

Published for SISSA by Springer

Received: April 3, 2018
Revised: August 3, 2018
Accepted: September 10, 2018
Published: September 12, 2018

Singlet scalar and 2HDM extensions of the Standard Model: CP-violation and constraints from $(g-2)_\mu$ and eEDM

Venus Keus,[a,b] **Niko Koivunen**[a] **and Kimmo Tuominen**[a]

[a] *Department of Physics and Helsinki Institute of Physics, Gustaf Hallstromin katu 2, FIN-00014 University of Helsinki, Finland*

[b] *School of Physics and Astronomy, University of Southampton, Southampton, SO17 1BJ, United Kingdom*

E-mail: venus.keus@helsinki.fi, niko.koivunen@helsinki.fi, kimmo.i.tuominen@helsinki.fi

Abstract: We study popular scalar extensions of the Standard Model, namely the singlet extension, the 2-Higgs doublet model (2HDM) and its extension by a singlet scalar. We focus on the contributions of the added scalars to the anomalous magnetic moment of the muon, $(g-2)_\mu$ in the presence of CP-violation, and the electric dipole moment of the electron (eEDM) in these models. In the absence of CP-violation, CP-even and CP-odd scalars contribute with an opposite sign to the anomalous magnetic moment of the muon and as a result these models generally require very light scalars to explain the observed discrepancy in $(g-2)_\mu$. We study the effect of CP-violation on the anomalous magnetic moment of the muon and its compatibility with the eEDM constraints. We show that given the current status of the global set of constraints applied on all values of $\cot\beta$, in the CP-violating scalar extensions, there exist no viable parameter space in agreement with both a_μ and eEDM bounds.

Keywords: Beyond Standard Model, CP violation, Higgs Physics

ArXiv ePrint: 1712.09613

https://doi.org/10.1007/JHEP09(2018)059

JHEP09(2018)059

Contents

JHEP09(2018)059

1 Introduction

While the Standard Model (SM) of particle physics agrees very well with data from high energy collider experiments, it still falls short on explaining several observed features of Nature. For example, SM does not provide sufficient amount of CP-violation to source the Baryon Asymmetry of the Universe (BAU) [1] and the scalar sector of the SM does not provide a first order phase transition [2], which would be needed to produce BAU at the electroweak transition. Another example is the need to understand the origin of neutrino masses and mixing patterns. One possible paradigm to address these issues is to enlarge the scalar sector of the SM. Many such extensions have been studied in the literature [3–9].

In addition to providing new sources for CP-violation, the extra scalars arising from such extensions could also help to explain the muon anomalous magnetic moment $a_\mu = (g-2)_\mu/2$ which deviates from the SM prediction by

$$\Delta a_\mu = a_\mu^{\text{exp}} - a_\mu^{\text{SM}} = (2.87 \pm 0.8) \times 10^{-9} \ (3.6\sigma) \tag{1.1}$$

according to the most recent experiment done at BNL [10, 11].

Finally, extended scalar sectors provide new scalar mass eigenstates which can, for example, provide a Dark Matter (DM) candidate. Typically their stability is guaranteed by an ad-hoc discrete symmetry. In this paper, we do not consider a DM candidate and therefore, in the models we study we try to avoid extra symmetries if possible.

We focus on the following well-known scalar extensions of the SM

- Real and Complex Singlet extension of the SM (SM+RS, SM+CS)
- 2-Higgs-doublet model (2HDM)
- Complex Singlet extension of the 2HDM (2HDM+CS)

For each model, we calculate the contribution of the scalars to a_μ to see if they can explain the observed discrepancy.

$$\Delta a_\mu = a_\mu^{\text{exp}} - \left(a_\mu^{\text{SM (without scalars)}} + a_\mu^{\text{scalars}}\right) = 0 \Rightarrow a_\mu^{\text{scalars}} = (2.88 \pm 0.8) \times 10^{-9}. \tag{1.2}$$

We show that in the CP-conserving limit, due to the cancelling effect of the CP-odd and CP-even scalars, one can not explain the excess in eq. (1.2), unless very light scalars are present and $\tan\beta$ is very large. However, when CP-violation is introduced, we show that less dramatic values of $\tan\beta$ or scalar masses are required to produce the observed a_μ.

Having introduced CP-violation, the parameter space of models under consideration is strongly constrained by the data from ACME collaboration on electron and neutron Electric Dipole Moment (EDM) [12]. The bounds on electron EDM (eEDM) with

$$d_e < 10.25 \times 10^{-29} \text{ e cm} = 1.573 \times 10^{-15} \text{ GeV}^{-1}, \tag{1.3}$$

impose the strongest constraints on any Beyond Standard Model (BSM) scenario with CP-violation. In each of the models under consideration we study if the amount of CP-violation required to explain the a_μ discrepancy can be accommodated within the limits imposed by

JHEP09(2018)059

eq. (1.3). As CP-violation is one of the main ingredients of BAU, the identification of the surviving regions of the parameter space after imposing the eEDM bounds is a necessary prerequisite of BAU studies. The models we have listed above have appeared in the context of electroweak baryogenesis: for a singlet extension of the SM, see e.g. [13–16], for 2HDM see e.g. [17–25] and for a singlet extension of the 2HDM see [6, 26, 27]. In this paper, we show, for the first time, how to implement the constraints from eEDMs and from the muon anomalous moment systematically on these models. In particular we show how this allows to determine the experimentally favoured patterns of Yukawa interactions in these models.

The paper is organised as follows: for the reader's convenience, in section 2 we review the computation of a_μ and eEDM from a generic Lagrangian and show in detail the 1-loop and 2-loop calculations of such contributions. In sections 3, 4 and 5 we present the scalar potential, theoretical and experimental constraints and a_μ and d_e contributions in the SM+RS, SM+CS, 2HDM and 2HDM+CS scenarios, respectively. In section 6 we draw our conclusions and present our outlook.

2 Calculation of a_μ and d_e contributions

By definition, the $a_\mu = (g-2)_\mu/2$ and eEDM contributions are

$$\mathcal{L}_{a_\mu} = \frac{e}{2m_\mu}\, a_\mu\, (\bar{\mu}\sigma_{\mu\nu}\mu)F^{\mu\nu}, \tag{2.1}$$

$$\mathcal{L}_{d_e} = -\frac{i}{2}\, d_e\, (\bar{e}\sigma_{\mu\nu}\,\gamma_5 e)F^{\mu\nu}, \tag{2.2}$$

where $F_{\mu\nu}$ is the electromagnetic field strength and $\sigma_{\mu\nu} = i[\gamma_\mu, \gamma_\nu]/2$. Therefore, the relevant parts of the Lagrangian are

$$\mathcal{L} \supset \frac{e\, m_l}{8\pi^2}\left[c_L(\bar{l}\sigma_{\mu\nu}P_L l)F^{\mu\nu} + c_R(\bar{l}\sigma_{\mu\nu}P_R l)F^{\mu\nu}\right] + \text{h.c.}, \tag{2.3}$$

where l stands for the relevant lepton (e for eEDM calculations and μ for the muon anomalous magnetic moment). Expanding the Lagrangian for the explicit forms of the operators, leads to

$$\begin{aligned}\mathcal{L} &\supset \frac{e\, m_l}{8\pi^2}(c_L + c_R^*)(\bar{l}\sigma_{\mu\nu}P_L l)F^{\mu\nu} + \frac{e\, m_l}{8\pi^2}(c_L^* + c_R)(\bar{l}\sigma_{\mu\nu}P_R l)F^{\mu\nu} \\ &= \frac{e\, m_l}{8\pi^2}\,\mathrm{Re}(c_L + c_R^*)\,(\bar{l}\sigma_{\mu\nu}l)F^{\mu\nu} - i\frac{e\, m_l}{8\pi^2}\,\mathrm{Im}(c_L + c_R^*)\,(\bar{l}\sigma_{\mu\nu}\gamma_5 l)F^{\mu\nu}\end{aligned} \tag{2.4}$$

where $P_L = (1-\gamma_5)/2$ and $P_R = (1+\gamma_5)/2$ are the left and right projection operators. One, therefore, needs to explicitly calculate

$$a_\mu = \frac{m_\mu^2}{4\pi^2}\,\mathrm{Re}(c_L + c_R^*). \tag{2.5}$$

$$d_e = \frac{e\, m_e}{4\pi^2}\,\mathrm{Im}(c_L + c_R^*), \tag{2.6}$$

where c_L and c_R are the Wilson coefficients to be calculated for each loop diagram in figure 1 separately.

JHEP09(2018)059

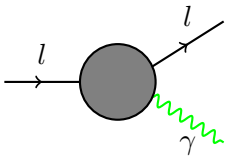

Figure 1. The higher order diagrams contributing to muon anomalous magnetic moment ($l = \mu$) and to eEDM ($l = e$).

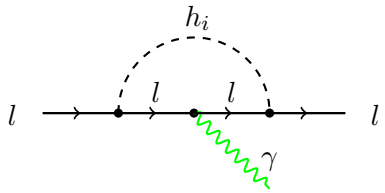

Figure 2. The 1-loop diagram mediated by neutral scalars h_i contributing to muon anomalous magnetic moment ($l = \mu$) and to eEDM ($l = e$).

2.1 1-loop contributions

The digram contributing to the a_μ and d_e at 1-loop is shown in figure 2, where h_i are the neutral scalars in the model with their coupling to electrons and muons represented by $Y_{ee}^{h_i}$ and $Y_{\mu\mu}^{h_i}$, respectively. The charged scalar mediated version of this diagram is sub-dominant and is therefore neglected [28]. The mass of the charged scalar is set to be equal to the mass of the heaviest scalar to comply with the ElectroWeak precision data. Note also that in the models we study, we only extend the scalar sector of SM and do not add any extra vector or fermion fields, such as right-handed neutrinos.

The Wilson coefficients are calculated to be

$$c_R = -\frac{Y_{ll}^{h_i}}{4m_l}\int_0^1 dx\int_0^x dy\,\frac{Y_{ll}^{h_i\,*}y(y-1)m_l + \lambda_{ll}^{h_i}(y-1)m_l}{m_l^2[y(y-x)+(1-y)]+m_{h_i}^2 y},$$
$$c_L = -\frac{Y_{ll}^{h_i\,*}}{4m_l}\int_0^1 dx\int_0^x dy\,\frac{Y_{ll}^{h_i}y(y-1)m_l + \lambda_{ll}^{h_i\,*}(y-1)m_l}{m_l^2[y(y-x)+(1-y)]+m_{h_i}^2 y}, \tag{2.7}$$

where $Y_{ll}^{h_i}$ is the scalar h_i's coupling to ll and could in general be complex,

$$Y_{ll}^{h_i} = \mathrm{Re}(Y_{ll}^{h_i}) + i\mathrm{Im}(Y_{ll}^{h_i}). \tag{2.8}$$

The contribution from the 1-loop diagrams to a_μ and d_e are then caluclated to be

$$a_\mu^{\text{1-loop}} = -\frac{m_\mu^2}{8\pi^2}\sum_{i=1}^{n}\int_0^1 dx\int_0^x dy\frac{y(y-1)\mid Y_{\mu\mu}^{h_i}\mid^2 + (y-1)\mathrm{Re}((Y_{\mu\mu}^{h_i})^2)}{m_\mu^2[y(y-x)+(1-y)]+m_{h_i}^2 y}, \tag{2.9}$$

$$d_e^{\text{1-loop}} = \frac{e\,m_e}{16\pi^2}\sum_{i=1}^{n}\mathrm{Im}((Y_{ee}^{h_i})^2)\int_0^1 dx\int_0^x dy\frac{(y-1)}{m_e^2[y(y-x)+(1-y)]+m_{h_i}^2 y}, \tag{2.10}$$

where n is the number of the scalars mediating the loop in figure 2. Our formulas are in agreement with the known results in [7, 28]–[29].

JHEP09(2018)059

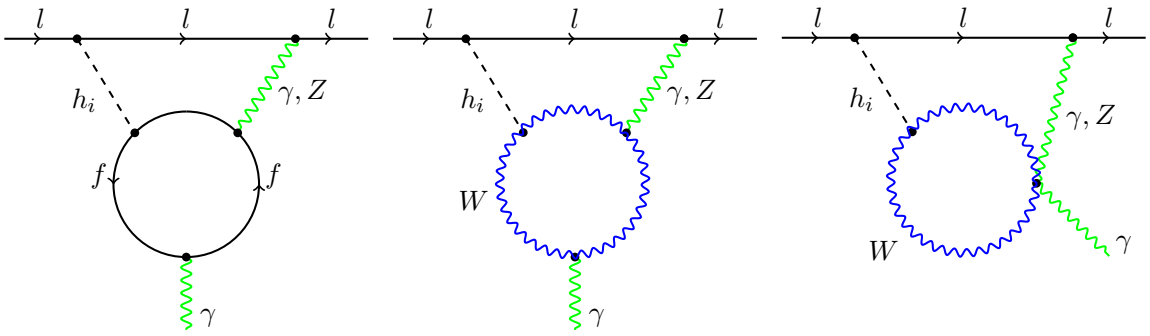

Figure 3. The Barr-Zee diagrams with largest contributions to muon anomalous magnetic moment ($l = \mu$) and eEDM ($l = e$).

2.2 2-loop contributions

The main 2-loop contributions to a_μ and d_e, shown in figure 3, arise from the Bar-Zee diagrams mediated by the scalar states.

The diagrams with the Z boson in the loop (instead of γ) are suppressed by a factor of $(\frac{1}{4} - \sin^2\theta_W)$, which makes their contribution almost two orders of magnitude smaller than diagrams with a photon in the loop. We therefore ignore such diagrams in the calculations that follow. Similarly, contributions from the charged scalars are ignored since they too are sub-dominant [30]. For our 2-loop calculations, we use the results of [31].

The contribution from 2-loop diagrams with heavy fermions ($f = t, b, c, \tau$),[1] and W to the a_μ are

$$a_{\mu,\ f}^{\text{2-loop}} = \frac{2}{3}\left(\frac{\alpha G_F v^2 m_\mu}{\sqrt{2}\pi^3 m_f}\right)\sum_{i=1}^{n}\left[\text{Re}(Y_{\mu\mu}^{h_i})\text{Re}(Y_{ff}^{h_i})f(z_{fh_i}) - \text{Im}(Y_{\mu\mu}^{h_i})\text{Im}(Y_{ff}^{h_i})g(z_{fh_i})\right], \tag{2.11}$$

$$a_{\mu,\ W}^{\text{2-loop}} = -\left(\frac{\alpha G_F v m_\mu}{4\sqrt{2}\pi^3}\right)\sum_{i=1}^{n}\frac{Y_{WW}^{h_i}}{2m_W^2/v}\text{Re}(Y_{\mu\mu}^{h_i})\left[3f(z_{Wh_i}) + \frac{23}{4}g(z_{Wh_i}) + \frac{3}{4}h(z_{Wh_i}) + \frac{f(z_{Wh_i}) - g(z_{Wh_i})}{2z_{Wh_i}}\right],$$

where $z_{AB} = m_A^2/m_B^2$, $Y_{WW}^{h_i}$ is the scalar h_i's coupling to WW. For the SM-Higgs coupling to WW, we use the notation $Y_{WW}^{h^{\text{SM}}}$ which in the pure SM limit is $2m_W^2/v$. The $Y_{ff}^{h_i}$ is the scalar h_i's coupling to ff which could in general be complex,

$$Y_{ff}^{h_i} = \text{Re}(Y_{ff}^{h_i}) + i\text{Im}(Y_{ff}^{h_i}), \tag{2.12}$$

and in the pure SM limit is m_f/v.

The contribution from 2-loop diagrams to the d_e from heavy fermions, f, and W loops are

$$d_{e,\ f}^{\text{2-loop}} = \frac{e}{3\pi^2}\left(\frac{\alpha G_F v^2}{\sqrt{2}\pi m_f}\right)\sum_{i=1}^{n}\left[\text{Im}(Y_{ee}^{h_i})\text{Re}(Y_{ff}^{h_i})f(z_{fh_i}) + \text{Re}(Y_{ee}^{h_i})\text{Im}(Y_{ff}^{h_i})g(z_{fh_i})\right], \tag{2.13}$$

$$d_{e,\ W}^{\text{2-loop}} = -\frac{e}{8\pi^2}\left(\frac{\alpha G_F v}{\sqrt{2}\pi}\right)\sum_{i=1}^{n}\frac{Y_{WW}^{h_i}}{2m_W^2/v}\text{Im}(Y_{ee}^{h_i})\left[3f(z_{Wh_i}) + \frac{23}{4}g(z_{Wh_i}) + \frac{3}{4}h(z_{Wh_i}) + \frac{f(z_{Wh_i}) - g(z_{Wh_i})}{2z_{Wh_i}}\right].$$

[1] The subscript f stands for fermion and is not to be confused with the loop function $f(z)$.

JHEP09(2018)059

The loop functions $f(z)$, $g(z)$ and $h(z)$ appearing in eqs. (2.11) and (2.13) and are presented in appendix A.

3 The real singlet extension (SM+RS)

The real singlet model is often presented with a Z_2 symmetry imposed on the scalar potential in order to stabilise the singlet field as a viable DM candidate [4, 32–35]. As mentioned earlier, in this paper we shall not look into DM phenomenology and hence we consider the model in its general form with no extra symmetries.

The most general potential in this case has the following form

$$\begin{aligned} V = &-\mu_1^2\Phi^\dagger\Phi - \mu_2^2 S^2 + \lambda_1(\Phi^\dagger\Phi)^2 + \lambda_2 S^4 + \lambda_3(\Phi^\dagger\Phi)S^2 \\ &+ \kappa_1 S + \kappa_2 S(\Phi^\dagger\Phi) + \kappa_3 S^3. \end{aligned} \tag{3.1}$$

Note that by a translation of S, the linear κ_1 term can be removed. The fields Φ and S are, respectively, the SM gauge doublet and singlet with Vacuum Expectation Values (VEVs) v and w. Their field decomposition is as follows,

$$\Phi = \begin{pmatrix} G^+ \\ \frac{v+\phi_1+iG^0}{\sqrt{2}} \end{pmatrix}, \quad S = \left(\frac{w+\phi_2}{\sqrt{2}}\right). \tag{3.2}$$

Since S is an SU(2) singlet, it has no direct couplings to the SM gauge bosons or fermions. The field Φ plays the role of the SM Higgs doublet, therefore, G^+ and G^0 are the would-be Goldstone bosons which are "eaten" by the $W^\pm$ and Z bosons.

The minimum of the potential requires

$$\begin{aligned} \mu_1^2 &= \frac{1}{2}\left(2\lambda_1 v^2 + \lambda_3 w^2 + \sqrt{2}\kappa_2 w\right), \\ \mu_2^2 &= \frac{1}{4w}\left(2\sqrt{2}\kappa_1 + \sqrt{2}\kappa_2 v^2 + 2\lambda_3 v^2 w + 4\lambda_2 w^3 + 3\sqrt{2}\kappa_3 w^2\right). \end{aligned} \tag{3.3}$$

The gauge eigenstates $\phi_{1,2}$ are then rotated to the mass eigenstates $h_{1,2}$ with the rotation matrix R defined as

$$\phi_i = R_{ij}h_j, \quad \begin{pmatrix} \phi_1 \\ \phi_2 \end{pmatrix} = \begin{pmatrix} \cos\theta & \sin\theta \\ -\sin\theta & \cos\theta \end{pmatrix} \begin{pmatrix} h_1 \\ h_2 \end{pmatrix}, \tag{3.4}$$

where we take h_1 to be the observed 125 GeV Higgs boson. The mixing angle θ is calculated to be

$$\tan(2\theta) = \frac{4vw\left(\sqrt{2}\kappa_2 + 2\lambda_3 w\right)}{2\sqrt{2}\kappa_1 + v^2\left(8\lambda_1 w + \sqrt{2}\kappa_2\right) - w^2\left(8\lambda_2 w + 3\sqrt{2}\kappa_3\right)}. \tag{3.5}$$

The value of $\sin\theta$ is bounded by experimental [36] and theoretical [37] constraints to be

$$|\sin\theta| < 0.33. \tag{3.6}$$

Throughout this paper we take the conservative limit of $\sin\theta \lesssim 0.3$ into account.

JHEP09(2018)059

Note that the two neutral scalar mass eigenstates, $h_{1,2}$, are a mixture of $\phi_{1,2}$ which are CP-even. Clearly there is no possibility of introducing CP-violation explicitly (through complex parameters in the potential) or spontaneously (through a complex VEV of the doublet and/or singlet). Hence, CP-violation is introduced through a higher dimension operator [5, 38]. In the absence of a Z_2 symmetry, we take this to be the following dimension-5 operator,

$$\mathcal{L}_{\rm CPV} = \frac{\eta}{\Lambda}\, S\, \bar{Q}_L\, \tilde{\Phi}\, t_R + \text{h.c.} \tag{3.7}$$

where

$$\eta = \text{Re}\eta + i\text{Im}\eta, \tag{3.8}$$

is the complex CP-violating parameter, Λ is the scale of new physics generating the effective operator, Q_L and t_R are, respectively, the left-handed doublet and right-handed quarks of the SM. Note that the sole source of CP-violation here is the parameter η, which is only introduced for the top quark couplings.

We use the conventional SM Yukawa couplings as defined by the Lagrangian,

$$\mathcal{L}_{\rm Yukawa} = Y^f_{ii}\, \bar{f}_{L,i} f_{R,i} \phi_1 + \text{h.c.}, \tag{3.9}$$

where, as clarified before, ϕ_1 is the SM Higgs field.

To calculate a_μ and d_e discussed in section 2, one needs to identify the couplings of the mass eigenstates $h_{1,2}$ to leptons, quarks and the W boson. These are:

$$Y^{h_i}_{ll} = R_{1i}\left(\frac{m_l}{v}\right) \qquad (l = \mu \text{ for } a_\mu, \quad l = e \text{ for } d_e) \tag{3.10}$$

$$Y^{h_i}_{WW} = R_{1i}\left(\frac{2m_W^2}{v}\right), \qquad Y^{h_i}_{qq} = R_{1i}\left(\frac{m_q}{v}\right) \tag{3.11}$$

$$Y^{h_i}_{tt} = R_{1i}\left(\frac{m_t}{v}\right) + R_{2i}\left(\frac{v(\text{Re}\eta + i\text{Im}\eta)}{2\Lambda}\right), \tag{3.12}$$

where R_{ij} are the components of the rotation matrix defined in eq. (3.4). Note that the only complex coupling is $Y^{h_i}_{tt} = \text{Re}(Y^{h_i}_{tt}) + i\text{Im}(Y^{h_i}_{tt})$ with

$$\text{Re}(Y^{h_i}_{tt}) = R_{1i}\left(\frac{m_t}{v}\right) + R_{2i}\left(\frac{v\text{Re}\eta}{2\Lambda}\right), \qquad \text{Im}(Y^{h_i}_{tt}) = R_{2i}\left(\frac{v\text{Im}\eta}{2\Lambda}\right). \tag{3.13}$$

Following from eq. (2.9)–(2.13), one can see that since $\text{Im}(Y^{h_i}_{ll}) = 0$, only the imaginary part of η contributes to d_e and only the real part to a_μ,

$$d_e \propto \text{Im}\eta, \qquad a_\mu \propto \text{Re}\eta, \tag{3.14}$$

as it will be shown in detail in the next two subsections. We will therefore quantify our results in terms of the dimensionless quantities $v\text{Re}(\eta)/(2\Lambda)$ for a_μ and $v\text{Im}(\eta)/(2\Lambda)$ for d_e. For the theoretical and experimental constraints, we have adopted the results in [37].

JHEP09(2018)059

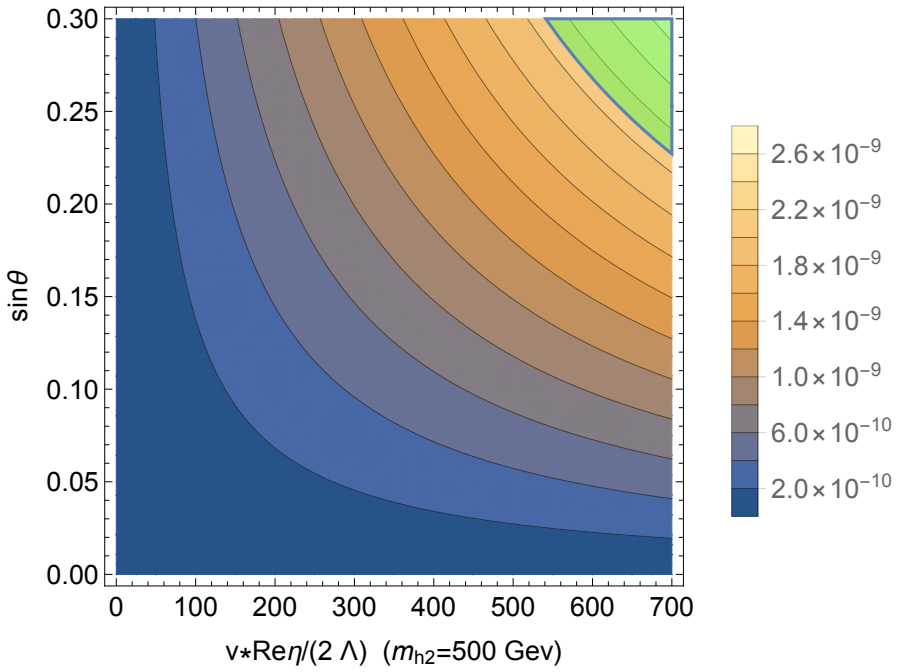

Figure 4. The contours showing a_μ in the SM+RS model. The green region is where the model produces a_μ within the observed window in eq. (1.2). At $\eta = 0$, where there is no $\mathcal{L}_{\rm CPV}$, the model does not provide large enough contribution to a_μ.

3.1 a_μ in the SM+RS model

As shown in detail in section 2, a_μ is proportional to the real part of the fermion-scalar couplings. Hence, all 1-loop and 2-loop contributions are non-zero and calculated to be

$$a_\mu^{\text{1-loop}} = -\frac{m_\mu^4}{8\pi^2 v^2}\sum_{i=1}^{2}\int_0^1 dx\int_0^x dy\frac{(y+1)(y-1)R_{1i}^2}{m_\mu^2\Big[y(y-x)+(1-y)\Big]+m_{h_i}^2 y}, \tag{3.15}$$

$$a_{\mu,\,t}^{\text{2-loop}} = \frac{2}{3}\left(\frac{\alpha G_F v m_\mu^2}{\sqrt{2}\pi^3 m_t}\right)\sum_{i=1}^{2}\left[R_{1i}\left(R_{1i}\left(\frac{m_t}{v}\right)+R_{2i}\left(\frac{v\text{Re}\eta}{2\Lambda}\right)\right)f(z_{th_i})\right],$$

$$a_{\mu,\,W}^{\text{2-loop}} = -\left(\frac{\alpha G_F m_\mu^2}{4\sqrt{2}\pi^3}\right)\sum_{i=1}^{2}R_{1i}^2\left[3f(z_{Wh_i})+\frac{23}{4}g(z_{Wh_i})+\frac{3}{4}h(z_{Wh_i})+\frac{f(z_{Wh_i})-g(z_{Wh_i})}{2z_{Wh_i}}\right],$$

$$a_{\mu,\,f}^{\text{2-loop}} = \frac{2}{3}\left(\frac{\alpha G_F m_\mu^2}{\sqrt{2}\pi^3}\right)\sum_{i=1}^{2}\left[R_{1i}^2 f(z_{fh_i})\right], \quad (f\neq t)$$

where $R_{11} = \cos\theta$ and $R_{12} = \sin\theta$ are the elements of the rotation matrix in eq. (3.4).

We find that SM+RS model is incapable of explaining the muon anomalous moment for m_{h_2} of a few hundred GeV, even in the presence of a non-zero $\mathcal{L}_{\rm CPV}$. In figure 4, we show contours of a_μ in the $\sin\theta$-$v\text{Re}(\eta)/(2\Lambda)$-plane for a representative value of $m_{h_2} = 500\,\text{GeV}$. The green region is where the model produces a_μ within the observed window in eq. (1.2). Hence, one would need a very large, $\mathcal{O}(10^3)$, non-trivial coupling to top quark in eq. (3.7).

JHEP09(2018)059

Note that the green region shown in the plot is not affected by eEDM constraints, which are governed by different couplings. We will discuss these constraints in detail in the next section.

3.2 d_e in the SM+RS model

As mentioned before, the only CP-violating coupling is that of the top quark which is introduced in eq. (3.7) through a dimension-5 operator. Therefore the only eEDM contributions come from the 2-loop Barr-Zee diagrams mediated by the top quark as the 1-loop and W-mediated 2-loop diagrams are proportional to the imaginary part of the scalar-electron couplings and are hence zero,

$$d_e^{\text{1-loop}} \propto \text{Im}((Y_{ee}^{hi})^2) = 0, \quad \text{and} \quad d_{e,\,W}^{\text{2-loop}} \propto \text{Im}(Y_{ee}^{hi}) = 0. \tag{3.16}$$

From eq. (2.13), the 2-loop contributions from the top quark are calculated to be

$$d_{e,\,t}^{\text{2-loop}} = \frac{e}{3\pi^2}\left(\frac{\alpha G_F v}{\sqrt{2}\pi m_t}\right) m_e \left(\frac{v\text{Im}\eta}{2\Lambda}\right) \sin\theta\cos\theta\left[-g(z_{th_1}) + g(z_{th_2})\right]. \tag{3.17}$$

In figure 5, we show contours of d_e in the $\sin\theta$-$(v\text{Im}\eta/2\Lambda)$-plane. The superimposed red regions are ruled out by the experimental bound in eq. (1.3). In the left panel of the figure $m_{h_2} = 140\,\text{GeV}$ and in the right panel $m_{h_2} = 500\,\text{GeV}$. As predicted by eq. (3.17), when $m_{h_2} \approx m_{h_1} = 125\,\text{GeV}$, and $g(z_{th_1}) \approx g(z_{th_2})$, the 2-loop contributions to d_e are reduced. Hence, as m_{h_2} approaches m_{h_1}, a larger region of the parameter space will survive the eEDM bounds as shown by the smaller excluded red area in the left panel of figure 5 in comparison to the right panel.

3.3 Remark on complex singlet extension

The results derived in the previous subsections are directly applicable also to the case where SM is extended by a complex singlet scalar (SM+CS). It has been shown [39] that an apparent CP violating phase in a model with a scalar doublet and a complex singlet scalar can be rotated away, and no explicit or spontaneous CP violation can be introduced in the SM+CS model. Similar to the SM+RS model, the only CP violation would come from higher dimensional operators such as in eq. (3.7).

The SM doublet Φ and SM singlet S are defined as:

$$\Phi = \begin{pmatrix} G^+ \\ \frac{1}{\sqrt{2}}\left(v + \phi_1 + iG^0\right) \end{pmatrix}, \quad S = \left(\frac{w + \phi_2 + i\phi_3}{\sqrt{2}}\right), \tag{3.18}$$

with v and w as VEVs of the doublet and the singlet, respectively. Similar to the SM+RS case, Φ is the SM Higgs doublet with $G^\pm$ and G^0 as the Goldstone bosons.

The gauge eigenstates $\phi_{1,2,3}$ are rotated to the mass eigenstates $h_{1,2,3}$ through

$$\phi_i = R_{ij}h_j, \quad \begin{pmatrix}\phi_1\\ \phi_2\\ \phi_3\end{pmatrix} = \begin{pmatrix}\cos\theta & \sin\theta & 0\\ -\sin\theta & \cos\theta & 0\\ 0 & 0 & 1\end{pmatrix}\begin{pmatrix}h_1\\ h_2\\ h_3\end{pmatrix}. \tag{3.19}$$

JHEP09(2018)059

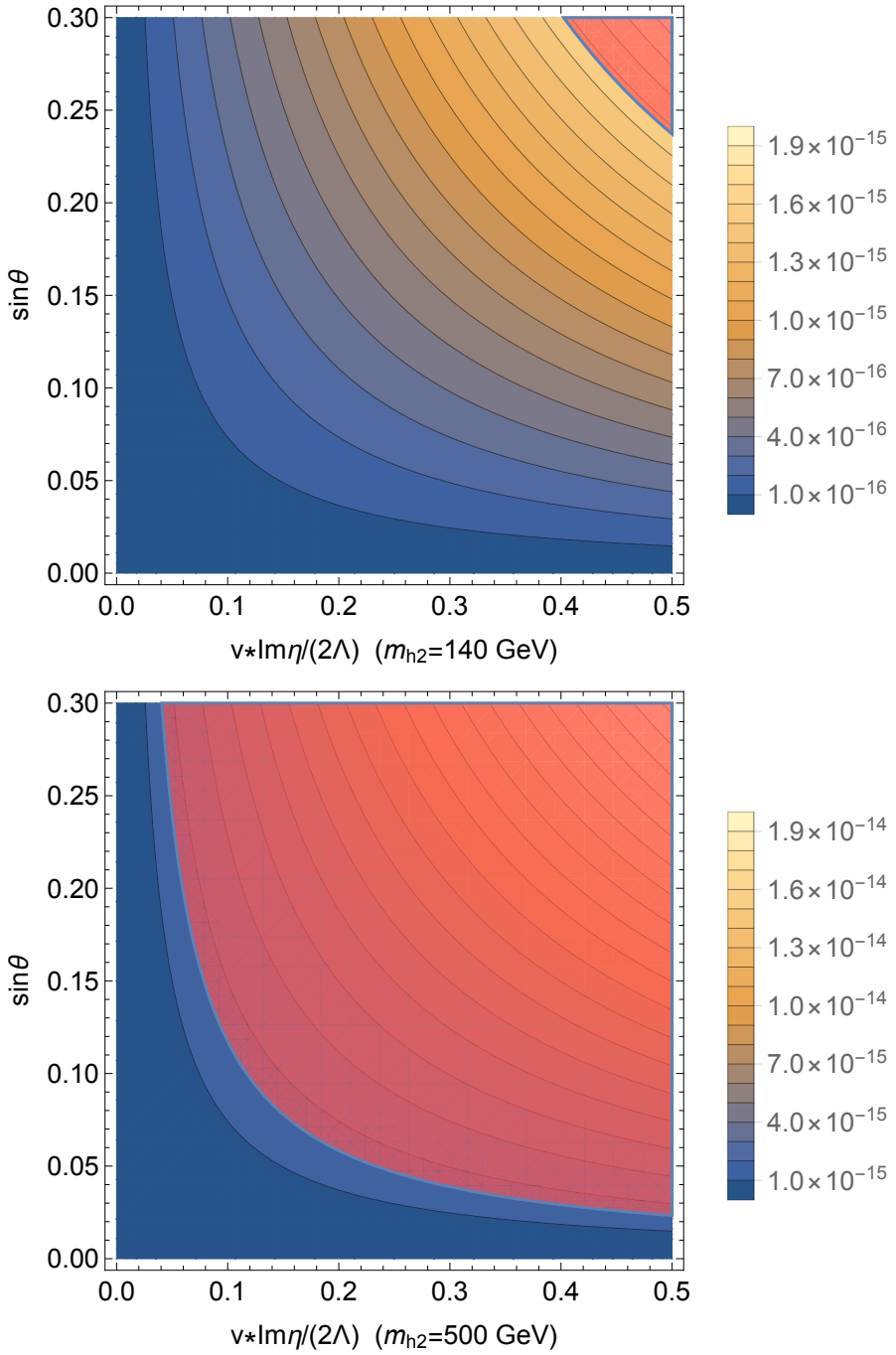

Figure 5. The contours showing the eEDM contributions in the SM+RS model for $m_{h_2} = 140$ (top) and $m_{h_2} = 500\,\text{GeV}$ (bottom). The red region is ruled out by experimental data.

Due to its singlet nature, ϕ_3 does not couple to the fermions and the W boson.[2] Therefore, ϕ_3 does not influence the calculations of the d_e and a_μ in comparison to the SM+RS model and the results are identical to the ones presented in the preceding section.

[2]Through the higher order operator, $\mathcal{L}_{\text{CPV}}$, ϕ_3 has a coupling to the top quark. However, it does not contribute to the Barr-Zee diagrams since it has no coupling to e and μ.

JHEP09(2018)059

4 The two Higgs doublet model (2HDM)

Extending the SM with one extra scalar doublet with the same SM quantum numbers as the SM-Higgs doublet,[3] one arrives at the well-studied 2HDM [40–46]. The most general 2HDM potential can be written in the following form:

$$\begin{aligned} V = &-\mu_1^2(\Phi_1^\dagger\Phi_1) - \mu_2^2(\Phi_2^\dagger\Phi_2) - \Big[\mu_3^2(\Phi_1^\dagger\Phi_2) + \text{h.c.}\Big] \\ &+ \lambda_1(\Phi_1^\dagger\Phi_1)^2 + \lambda_2(\Phi_2^\dagger\Phi_2)^2 + \lambda_3(\Phi_1^\dagger\Phi_1)(\Phi_2^\dagger\Phi_2) + \lambda_4(\Phi_1^\dagger\Phi_2)(\Phi_2^\dagger\Phi_1) \\ &+ \Big[\lambda_5(\Phi_1^\dagger\Phi_2)^2 + \lambda_6(\Phi_1^\dagger\Phi_1)(\Phi_1^\dagger\Phi_2) + \lambda_7(\Phi_2^\dagger\Phi_2)(\Phi_1^\dagger\Phi_2) + \text{h.c.}\Big]. \end{aligned} \tag{4.1}$$

In the general case, due to the existence of two scalar doublets to which fermions can couple, 2HDMs suffer from Flavour Changing Neutral Current interactions (FCNCs) at tree-level, which are strongly restricted experimentally. It is known that imposing a softly broken Z_2 symmetry on the scalar potential, and extending it to the fermion sector can forbid these FCNCs [47, 48]. Depending on the Z_2 charge assignment of the fermions, four independent types of Yukawa interactions are allowed, and these are known as Type-I, Type-II, Type-X (Lepton-specific) and Type-Y (Flipped) in the literature [41, 42, 49], and references therein. These will be discussed in section 4.2. In what follows, the transformation of the scalar doublets under this Z_2 symmetry is fixed to be $\Phi_1 \to +\Phi_1$ and $\Phi_2 \to -\Phi_2$.

Imposing the softly broken Z_2 symmetry forbids the $\lambda_{6,7}$ terms in the potential in eq. (4.1),

$$\lambda_6 = \lambda_7 = 0. \tag{4.2}$$

The rest of the parameters are real with the exception of μ_3^2 and λ_5 which are complex and defined as

$$\mu_3^2 = \text{Re}\mu_3^2 + i\ \text{Im}(\mu_3^2), \qquad \lambda_5 = \text{Re}\lambda_5 + i\ \text{Im}\lambda_5. \tag{4.3}$$

In this paper, we take the VEVs of the doublets to be real and positive and study explicit CP-violation which occurs when $\text{Im}(\lambda_5^*[\mu_3^2]^2) \neq 0$ [50], through the complex parameters of the potential.

In general, the decomposition of the scalar doublets is as follows

$$\Phi_1 = \begin{pmatrix} \phi_1^+ \\ \frac{v_1+h_1^0+ia_1^0}{\sqrt{2}} \end{pmatrix}, \quad \Phi_2 = \begin{pmatrix} \phi_2^+ \\ \frac{v_2+h_2^0+ia_2^0}{\sqrt{2}} \end{pmatrix}, \tag{4.4}$$

where v_1 and v_2 are taken to be real with $v^2 = v_1^2 + v_2^2 = (246\text{GeV})^2$ and, as usual, we define $\tan\beta = v_2/v_1$.

4.1 Minimisation of the 2HDM potential

The minimization of the potential implies

$$\begin{aligned} \mu_1^2 &= -\tan\beta\text{Re}\mu_3^2 + v^2 s_\beta^2 \text{Re}\lambda_5 + \frac{v^2}{4}\left(2\lambda_1 + \lambda_3 + \lambda_4 + c_{2\beta}(2\lambda_1 - \lambda_3 - \lambda_4)\right) \\ \mu_2^2 &= -\cot\beta\text{Re}\mu_3^2 + v^2 c_\beta^2 \text{Re}\lambda_5 + \frac{v^2}{4}\left(2\lambda_2 + \lambda_3 + \lambda_4 + c_{2\beta}(-2\lambda_2 + \lambda_3 + \lambda_4)\right) \\ \text{Im}\mu_3^2 &= v^2 s_\beta c_\beta \text{Im}\lambda_5, \end{aligned} \tag{4.5}$$

where s_β and c_β stand for $\sin\beta$ and $\cos\beta$, respectively.

[3] Note that extending the SM with a doublet with different charges, e.g. hypercharge, still leads to a 2HDM.

JHEP09(2018)059

At this point, it is useful to rotate the doublets to the so called Higgs basis [51],

$$\begin{pmatrix} \widehat{\Phi}_1 \\ \widehat{\Phi}_2 \end{pmatrix} = \begin{pmatrix} \cos\beta & \sin\beta \\ -\sin\beta & \cos\beta \end{pmatrix} \begin{pmatrix} \Phi_1 \\ \Phi_2 \end{pmatrix}, \tag{4.6}$$

where only one of the doublets has a VEV

$$\widehat{\Phi}_1 = \begin{pmatrix} G^+ \\ \frac{v+\phi_1+iG^0}{\sqrt{2}} \end{pmatrix}, \quad \widehat{\Phi}_2 = \begin{pmatrix} H^+ \\ \frac{\phi_2+i\phi_3}{\sqrt{2}} \end{pmatrix}, \tag{4.7}$$

and one can separate the Goldstone bosons, $G^\pm, G^0$, from the physical states. The mass of the charged Higgs is calculated to be

$$m^2_{H^\pm} = \frac{\mathrm{Re}\mu_3^2}{s_\beta c_\beta} - \frac{v^2}{2}(\lambda_4 + 2\mathrm{Re}\lambda_5). \tag{4.8}$$

The neutral mass-squared matrix, $\mathcal{M}^2$, shown in detail in appendix B, is a 3×3 matrix which is diagonalised by the rotation matrix R,

$$R^T\mathcal{M}^2R = \mathcal{M}^2_{\mathrm{diag}} = \mathrm{diag}(m^2_{h_1}, m^2_{h_2}, m^2_{h_3}), \tag{4.9}$$

where we take h_1 to be the observed Higgs boson at the LHC with $m_{h_1} = 125\,\mathrm{GeV}$.

The rotation matrix, R, depends on the three mixing angles, θ_{12}, θ_{13} and θ_{23}, where the latter two angles represent CP-violation and will vanish in the CP-conserving limit. Therefore, we take these angles to be small since, as it will be shown later, they prove to be very small in the interesting and allowed regions of the parameter space. The angle θ_{12} represents the mixing of the SM-like Higgs with the other CP-even state. As shown in eq. (3.6), to agree with the observed Higgs data, we take θ_{12} to be small.

With all mixing angles being small ($\cos\theta_i \simeq 1$ and $\sin\theta_i \simeq \theta_i$), the rotation matrix, R, simplifies to the form

$$\phi_i = R_{ij}h_j, \qquad \begin{pmatrix} \phi_1 \\ \phi_2 \\ \phi_3 \end{pmatrix} = \begin{pmatrix} 1 & \theta_{12} & \theta_{13} \\ -\theta_{12} & 1 & \theta_{23} \\ -\theta_{13} & -\theta_{23} & 1 \end{pmatrix} \begin{pmatrix} h_1 \\ h_2 \\ h_3 \end{pmatrix}. \tag{4.10}$$

With this simplified form, one can calculate the angles in terms of the parameters of the potential as shown in appendix B.

After minimisation, the 9 independent parameters of the model,

$$\mu_1^2,\ \mu_2^2,\ \mathrm{Re}\mu_3^2,\ \lambda_1,\ \lambda_2,\ \lambda_3,\ \lambda_4,\ \mathrm{Re}\lambda_5,\ \mathrm{Im}\lambda_5, \tag{4.11}$$

can be expressed in terms of

$$\tan\beta,\ v,\ m_{h_1},\ m_{h_2},\ m_{h_3},\ m_{H^\pm},\ \theta_{12},\ \theta_{13},\ \theta_{23}, \tag{4.12}$$

which we take as input parameters for our numerical calculations.

JHEP09(2018)059

	Φ_1	Φ_2	u_R	d_R	e_R	Q_L, L_L	ξ_d	ξ_u	ξ_l
Type-I	+	−	−	−	−	+	$\cot\beta$	$\cot\beta$	$\cot\beta$
Type-II	+	−	−	+	+	+	$-\tan\beta$	$\cot\beta$	$-\tan\beta$
Type-X	+	−	−	−	+	+	$\cot\beta$	$\cot\beta$	$-\tan\beta$
Type-Y	+	−	−	+	−	+	$-\tan\beta$	$\cot\beta$	$\cot\beta$

Table 1. Z_2 charge assignment and ξ-coefficients in the Yukawa couplings of d, u, l fermions in the four types of Yukawa interactions.

4.2 Yukawa and gauge couplings

In the general 2HDM, interactions of the scalar sector with SM fermions are defined as

$$-\mathcal{L}_Y = Y_u \bar{Q}'_L i\sigma_2 \Phi_u^* u'_R + Y_d \bar{Q}'_L \Phi_d d'_R + Y_e \bar{L}'_L \Phi_e e'_R + \text{h.c.}\,, \tag{4.13}$$

where $\Phi_{u,d,e}$ are Φ_1 and/or Φ_2 depending on the type of Yukawa interactions. This correspondence is determined according to table 1 after the Z_2 charge assignments for fermions have been specified.

Starting from eq. (4.13), one rotates $\Phi_{1,2}$ to $\widehat{\Phi}_{1,2}$ in the Higgs basis using eq. (4.6). The primed fermion gauge doublets and singlets, will have to be written in terms of the unprimed mass eigenstates using the usual unitary matrices U_L and U_R, which also diagonalise the fermion mass and Yukawa matrices simultaneously. The Yukawa interactions can then be written in the following compact form

$$\mathcal{L}_{Y_d} = \bar{d}_L \frac{m_d}{v} d_R \sum_i^3 \left(R_{1i} + \xi_d (R_{2i} + i\, R_{3i})\right) h_i, \tag{4.14}$$

$$\mathcal{L}_{Y_l} = \bar{e}_L \frac{m_l}{v} e_R \sum_i^3 \left(R_{1i} + \xi_l (R_{2i} + i\, R_{3i})\right) h_i, \tag{4.15}$$

$$\mathcal{L}_{Y_u} = \bar{u}_L \frac{m_u}{v} u_R \sum_i^3 \left(R_{1i} + \xi_u (R_{2i} - i\, R_{3i})\right) h_i, \tag{4.16}$$

where the R_{ij} are the rotation matrix elements defined in eq. (4.10) and the coefficients ξ_i are Type-specific as defined in table 1.

The scalar-gauge interactions are derived from the kinetic terms and are of the form

$$\begin{aligned} \mathcal{L}_{\text{kin}} =& \mid D_\mu \Phi_1 \mid^2 + \mid D_\mu \Phi_2 \mid^2 = \mid D_\mu \widehat{\Phi}_1 \mid^2 + \mid D_\mu \widehat{\Phi}_2 \mid^2 \\ \supset& \frac{2m_W^2}{v}\, \phi_1\, W_\mu W^\mu + \frac{m_Z^2}{v}\, \phi_1\, Z_\mu Z^\mu = R_{1i} h_i \left(\frac{2m_W^2}{v} W_\mu W^\mu + \frac{m_Z^2}{v} Z_\mu Z^\mu\right), \end{aligned} \tag{4.17}$$

where, again, R_{1i} are rotation matrix elements defined in eq. (4.10).

In all the results that follow, we take into account theoretical and experimental bounds as shown in detail in appendix C. For our plots, we find it instructive to show a large region of $\cot\beta$, and point out, in each subsection, the regions that are ruled out experimentally.

JHEP09(2018)059

4.3 a_μ and d_e in 2HDMs

4.3.1 General type-independent formulas for a_μ and d_e

The contribution from 1-loop diagrams to a_μ and d_e are

$$a_\mu^{\text{1-loop}} = -\frac{m_\mu^4}{8\pi^2 v^2}\sum_{i=1}^{3}\int_0^1 dx\int_0^x dy \frac{(y+1)(y-1)(R_{1i}+\xi_l R_{2i})^2+(y-1)^2(\xi_l R_{3i})^2}{m_\mu^2[y(y-x)+(1-y)]+m_{h_i}^2 y}, \tag{4.18}$$

$$d_e^{\text{1-loop}} = \frac{e\, m_e^3}{8\pi^2 v^2}\sum_{i=1}^{3}\xi_l R_{3i}(R_{1i}+\xi_l R_{2i})\int_0^1 dx\int_0^x dy \frac{(y-1)}{m_e^2[y(y-x)+(1-y)]+m_{h_i}^2 y}. \tag{4.19}$$

The 2-loop contributions from up-Type and down-Type quarks, leptons and the W boson to a_μ are

$$a_{\mu,\,u}^{\text{2-loop}} = \frac{2}{3}\left(\frac{\alpha G_F m_\mu^2}{\sqrt{2}\pi^3}\right)\sum_{i=1}^{3}\left[(R_{1i}+\xi_l R_{2i})(R_{1i}+\xi_u R_{2i})f(z_{uh_i})+\xi_l\xi_u R_{3i}^2 g(z_{uh_i})\right], \tag{4.20}$$

$$a_{\mu,\,d}^{\text{2-loop}} = \frac{2}{3}\left(\frac{\alpha G_F m_\mu^2}{\sqrt{2}\pi^3}\right)\sum_{i=1}^{3}\left[(R_{1i}+\xi_l R_{2i})(R_{1i}+\xi_d R_{2i})f(z_{dh_i})-\xi_l\xi_d R_{3i}^2 g(z_{dh_i})\right], \tag{4.21}$$

$$a_{\mu,\,l}^{\text{2-loop}} = \frac{2}{3}\left(\frac{\alpha G_F m_\mu^2}{\sqrt{2}\pi^3}\right)\sum_{i=1}^{3}\left[(R_{1i}+\xi_l R_{2i})^2 f(z_{lh_i})-\xi_l^2 R_{3i}^2 g(z_{lh_i})\right], \tag{4.22}$$

$$a_{\mu,\,W}^{\text{2-loop}} = -\left(\frac{\alpha G_F m_\mu^2}{4\sqrt{2}\pi^3}\right)\sum_{i=1}^{3}R_{1i}(R_{1i}+\xi_l R_{2i}) \times\left[3f(z_{Wh_i})+\frac{23}{4}g(z_{Wh_i})+\frac{3}{4}h(z_{Wh_i})+\frac{f(z_{Wh_i})-g(z_{Wh_i})}{2z_{Wh_i}}\right]. \tag{4.23}$$

The 2-loop contributions from up-Type and down-Type quarks, leptons and the W boson to d_e are

$$d_{e,\,u}^{\text{2-loop}} = \frac{e\alpha G_F m_e}{3\sqrt{2}\pi^3}\sum_{i=1}^{3}\left[\xi_l R_{3i}(R_{1i}+\xi_u R_{2i})f(z_{uh_i})-\xi_u R_{3i}(R_{1i}+\xi_l R_{2i})g(z_{uh_i})\right], \tag{4.24}$$

$$d_{e,\,d}^{\text{2-loop}} = \frac{e\alpha G_F m_e}{3\sqrt{2}\pi^3}\sum_{i=1}^{3}\left[\xi_l R_{3i}(R_{1i}+\xi_d R_{2i})f(z_{dh_i})+\xi_d R_{3i}(R_{1i}+\xi_l R_{2i})g(z_{dh_i})\right], \tag{4.25}$$

$$d_{e,\,l}^{\text{2-loop}} = \frac{e\alpha G_F m_e}{3\sqrt{2}\pi^3}\sum_{i=1}^{3}\left[\xi_l R_{3i}(R_{1i}+\xi_l R_{2i})f(z_{lh_i})+\xi_l R_{3i}(R_{1i}+\xi_l R_{2i})g(z_{lh_i})\right], \tag{4.26}$$

$$d_{e,\,W}^{\text{2-loop}} = -\frac{e\alpha G_F m_e}{8\sqrt{2}\pi^3}\sum_{i=1}^{3}R_{1i}\xi_l R_{3i}\left[3f(z_{Wh_i})+\frac{23}{4}g(z_{Wh_i})+\frac{3}{4}h(z_{Wh_i})+\frac{f(z_{Wh_i})-g(z_{Wh_i})}{2z_{Wh_i}}\right]. \tag{4.27}$$

Note that these results are *type-independent*: each type of 2HDM can be studied further numerically when the corresponding values of ξ_l, ξ_d and ξ_u presented in table 1 are implemented.

JHEP09(2018)059

4.3.2 The numerical formulas for a_μ and d_e for given masses

To gain insight into how the constraints on a_μ and d_e operate in different models, it is instructive to look at the explicit numerical form of the total a_μ and d_e contributions. Here, we present explicitly the numerical formulas for exemplary values of $m_{h_{2,3}} = 200, 300\,\text{GeV}$; of course, the formulas corresponding to any other mass texture can be easily produced from the general results presented in the preceding subsection.

The total contribution from the scalars to a_μ is

$$\begin{aligned} a_\mu = 10^{-11}\Big[&-1.7 + \xi_l\xi_u(2.2 + 1.4\theta_{12}^2 + 2.0\theta_{13}^2 + 2.3\theta_{23}^2) + \xi_l(0.8\theta_{12} - 0.3\theta_{13}\theta_{23}) \\ &+ \xi_u(-0.3\theta_{12} + 0.8\theta_{13}\theta_{23}) - 0.9\,\theta_{12}^2 - 0.3\,\theta_{13}^2 \\ &+ \xi_l\xi_d(0.5 + 3.2\theta_{12}^2 - 4.0\theta_{13}^2 - 1.1\theta_{23}^2) \times 10^{-2} + \xi_d(-0.1\theta_{12} + 0.8\theta_{13}\theta_{23}) \times 10^{-2} \\ &+ \xi_l^2(0.2 + 1.1\theta_{12}^2 - 1.3\theta_{13}^2 - 0.3\theta_{23}^2) \times 10^{-2}\Big], \end{aligned} \tag{4.28}$$

where the last two lines are the contributions of the down-Type quarks (mostly b) and charged leptons (mostly τ) to the Barr-Zee diagrams which clearly are sub-dominant. Hence, Type-I and Type-Y (and similarly, Type-II and Type-X), whose only difference is in ξ_d, contribute almost identically to d_e and a_μ, especially when $\xi_{l,d}$ are not very large as it will be clarified further here.

To see the exact difference between Type-I and Y (and similarly Type-II and X), we show the explicit numeric formulas in each case. For Type I,

$$a_\mu^{\text{I}} = 10^{-11}\Big[-1.7 + \cot^2\beta(2.2 + 1.4\theta_{12}^2 + 2\theta_{13}^2 + 2.3\theta_{23}^2) + \cot\beta(0.4\theta_{12} + 0.4\theta_{13}\theta_{23}) - 0.9\theta_{12}^2 - 0.3\theta_{13}^2\Big], \tag{4.29}$$

and for Type Y,

$$a_\mu^{\text{Y}} = a_\mu^{\text{I}} + 10^{-11}\left[\left(-0.5 + 4\theta_{13}^2 + \theta_{23}^2 + \cot^2\beta(-0.5 + \theta_{23}^2) + \tan\beta(\theta_{12} - 0.8\theta_{13}\theta_{23})\right) \times 10^{-2}\right], \tag{4.30}$$

which has a subdominant correction with respect to Type-I. Note that when $\tan\beta < 10^2$, this correction is negligibly small, as it is shown in figure 6. From these equations we see that Type-I (and Y) are capable of producing a large enough a_μ in the $\cot\beta \gtrsim 10$ region.

For Type II,

$$\begin{aligned} a_\mu^{\text{II}} = 10^{-11}\Big[&-3.9 + \cot\beta(-0.3\theta_{12} + 0.8\theta_{13}\theta_{23}) + \tan\beta(-0.8\theta_{12} + 0.3\theta_{13}\theta_{23}) \\ &- 2.3(\theta_{12}^2 + \theta_{13}^2 + \theta_{23}^2) + \tan^2\beta\left(0.7 + 4\theta_{12}^2 - 5\theta_{13}^2 - 1.3\theta_{23}^2\right) \times 10^{-2}\Big], \end{aligned} \tag{4.31}$$

and for Type X

$$a_\mu^{\text{X}} = a_\mu^{\text{II}} + 10^{-11}\left[\left(-0.5 + \theta_{23}^2 + \tan^2\beta(-0.5 - 3\theta_{12}^2 - 6\theta_{13}^2 + \theta_{23}^2)\right) \times 10^{-2}\right], \tag{4.32}$$

which again has a sub-dominant correction to Type-II. Note that when $\tan\beta < 10$, this correction is negligibly small. From these equations we see that Type-II (and X) are capable

JHEP09(2018)059

of producing a large enough a_μ in the $\cot\beta \gtrsim 100$ and $\tan\beta \gtrsim 100$ regions. These findings are summarised in figure 6, where we show the a_μ contributions in the CP-conserving limit ($\theta_{13} = \theta_{23} = 0$) on the top panel and in the presence of CP-violation on the middle panel.

On the other hand, keeping only the leading terms, the total eEDM contributions are

$$d_e = 10^{-14}\Big|\xi_l\Big(9.6\theta_{13}+6.6\theta_{23}\theta_{12}\Big)+\xi_u\Big(6.6\theta_{13}+10.6\theta_{23}\theta_{12}\Big)+\xi_l\xi_u\Big(0.8\theta_{23}-4.3\theta_{13}\theta_{12}\Big) \\ +\xi_d\Big(-0.2\theta_{13}-0.1\theta_{23}\theta_{12}\Big)+\xi_l\xi_d\Big(-0.1\theta_{23}+0.5\theta_{13}\theta_{12}\Big)+\xi_l^2\Big(-0.03\theta_{23}+0.1\theta_{13}\theta_{12}\Big)\Big|\,. \tag{4.33}$$

The bound in eq. (1.3) then gives the following constraints: for Type I,

$$\Big|\cot\beta(16\theta_{13}+17\theta_{23}\theta_{12})+\cot^2\beta(0.7\theta_{23}-3.6\theta_{13}\theta_{12})\Big| < 0.15\,, \tag{4.34}$$

and for Type Y,

$$\Big|\cot\beta(16.2\theta_{13}+17.2\theta_{23}\theta_{12})+\cot^2\beta(0.8\theta_{23}-4.1\theta_{13}\theta_{12}) \\ +\tan\beta(0.2\theta_{13}+0.1\theta_{23}\theta_{12})+0.1\theta_{23}-0.5\theta_{12}\theta_{13}\Big| < 0.15. \tag{4.35}$$

Note that the difference between the d_e contribution in Type-I and Y is proportional to $\tan\beta$ whose effect is visible in the low $\cot\beta$ region in figure 6.

To satisfy these constraints, in both Type-I and Y, one requires small $\cot\beta$. Note also that when $\cot\beta$ is small, $\tan\beta$ is large which makes the d_e-surviving region in Type-Y more constrained when compared to Type-I.

For Type II,

$$\Big|\cot\beta(6.6\theta_{13}+10.6\theta_{23}\theta_{12})+(-0.8\theta_{23}+4.3\ \theta_{13}\theta_{12}) \\ +\tan\beta(-9.4\theta_{13}-6.4\theta_{23}\theta_{12})+\tan^2\beta(-0.1\theta_{23}+0.6\theta_{13}\theta_{12})\Big| < 0.15\,. \tag{4.36}$$

For Type X,

$$\Big|\cot\beta(6.4\theta_{13}+10.4\theta_{23}\theta_{12})+(-0.7\theta_{23}+3.8\ \theta_{13}\theta_{12}) \\ +\tan\beta(-9.6\theta_{13}-6.6\theta_{23}\theta_{12})+\tan^2\beta(-0.03\theta_{23}+0.1\theta_{13}\theta_{12})\Big| < 0.15\,, \tag{4.37}$$

whose contributions are very similar to each other, with both types surviving the d_e constraints in the $\tan\beta \approx \cot\beta \approx 1$ region. The similarities of Type II and X are also visible in figure 6 where the two types only differ slightly in the low $\cot\beta$ region.

Superimposing the a_μ and d_e plots, one can see that with heavy scalars, it is not possible to have a large enough a_μ contribution with the amount of CP-violation that is allowed by the eEDM data.

We emphasize that the above numerical formulas are presented for exemplary values of masses $m_{h_{2,3}} = 200, 300\,\text{GeV}$. In the next subsection, we will analyse different mass hierarchies in more detail.

JHEP09(2018)059

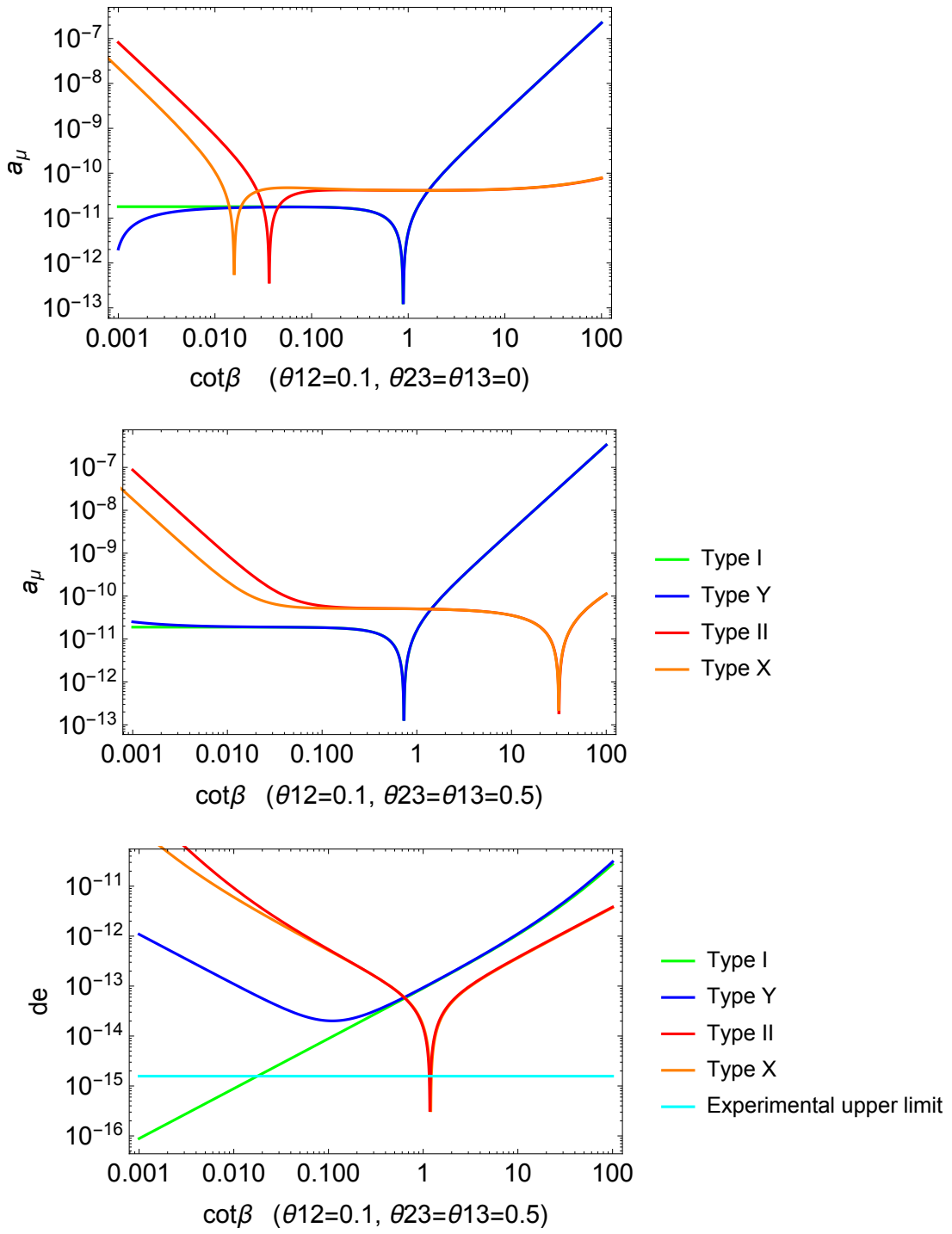

Figure 6. a_μ (top) and d_e (bottom) contribution in different 2HDM Types for fixed values of masses ($m_{h_{2,3}} = 200, 300\,\text{GeV}$) in the CP-conserving limit (left) and in the presence of CP-violation (right).

JHEP09(2018)059

4.4 2HDM results

We divide this section into three subsections dealing with heavy ($m_{h_{2,3}} \gtrsim m_{h_1}$), medium ($m_{h_{2,3}} \approx m_{h_1}$) and light ($m_{h_{2,3}} \lesssim m_{h_1}$) mass regions.

4.4.1 Heavy mass region

To investigate the effect of CP-violation more closely, in figure 7, we show the a_μ and d_e contributions for different values of the CP-violating angles, θ_{13} and θ_{23} for Type I and Type X for fixed scalar masses, $m_{h_{2,3}} = 200, 300\,\text{GeV}$. The black lines show the a_μ contribution of each model in the CP-conserving limit and the cyan line shows the experimental upper limit on the d_e contribution. Note that in Type I, larger CP-violating angles lead to larger a_μ values while the effect is more complicated and $\cot\beta$-dependent in Type X. Clearly with increasing CP-violation, the d_e contribution increases and the surviving region of the parameter space shrinks. As mentioned before, the behaviour of Type Y and II are, respectively, similar to Type I and X.

To study the effect of the scalar masses, in figure 8, we show the regions surviving the d_e constraint and regions producing a_μ within the observed band in Type I, Y, II and X 2HDMs for two sets of scalar masses and fixed values of $\theta_{12} = \theta_{23} = 0.1$. Types I and Y show the expected behaviour in agreement with figure 6: Type Y is more constrained by d_e in comparison to Type I due to the contribution proportional to $\tan\beta$ (see eq. (4.35)), which is large in small $\cot\beta$ region. However, the contributions to a_μ are almost identical in both types of models. Clearly the a_μ bands do not overlap with the d_e surviving regions in this case. Type II and X contribute almost identically to both a_μ and d_e: there are two regions, very small $\cot\beta$ and very large $\cot\beta$ which lead to the correct value for a_μ in agreement with figure 6. However, none of these regions pass the d_e bounds which are satisfied in the $\cot\beta \approx 1$ as also confirmed by figure 6.

Aside from the eEDM constraints, note that large values of $\cot\beta$ lead to large scalar-fermion couplings which are ruled out due to flavour and/or collider constraints. It has been shown in the CP-conserving limit in [29, 52–54] that due to these constraints only Type I and X models survive in the low $\cot\beta$ region.

4.4.2 Medium mass region

Next we turn to the medium mass region where all scalars have masses comparable with m_{h_1}. In figure 9, we show the behaviour of all four types of 2HDM over a large range of $\cot\beta$ values for fixed values of the angles. The behaviour is similar to the heavy mass region with a significant contribution to a_μ in the large $\cot\beta$ region in Type I, Y and in the small $\cot\beta$ region in Type II, X, both with and without CP-violation. The d_e contributions are also similar to the heavy scalar case with Type I, Y favouring the low $\cot\beta$ region while Type Y is more constrained, and with Type II, X leaning towards the $\cot\beta \approx 10$ region.

To get a closer look at the effect of CP-violation, we present in figure 10, a_μ and d_e contributions of Type I and X for fixed scalar masses and varying angles. Note that in Type I, larger CP-violating angles lead to larger a_μ values while the effect is more complicated and $\cot\beta$-dependent in Type X. Clearly with increasing CP-violation, the

JHEP09(2018)059

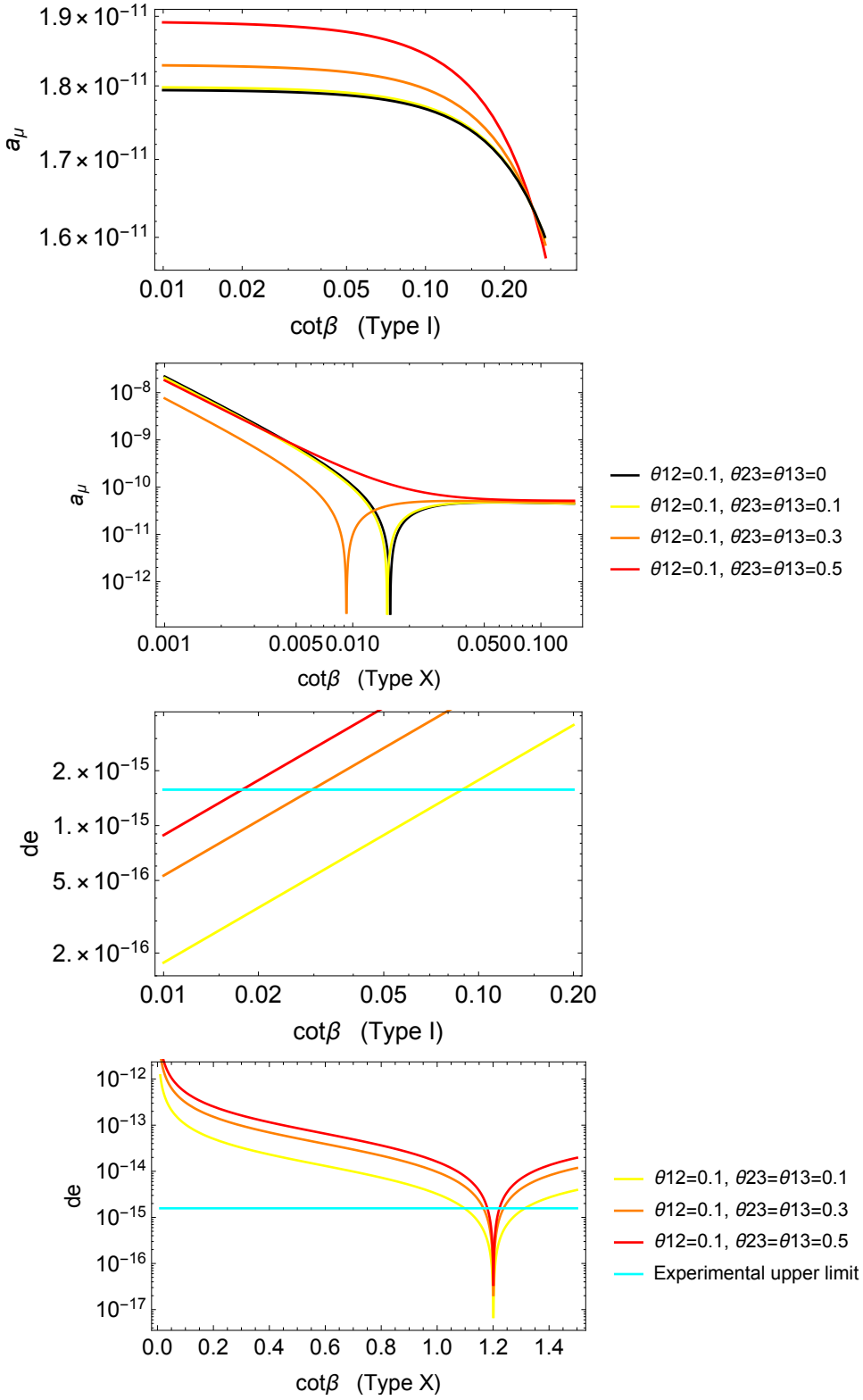

Figure 7. a_μ (top) and d_e (bottom) values in Type I (left) and Type X (right) for different values of angles and fixed values of masses ($m_{h_{2,3}} = 200, 300\,\text{GeV}$). The behaviour of Type Y and II are similar to Type I and X, respectively.

JHEP09(2018)059

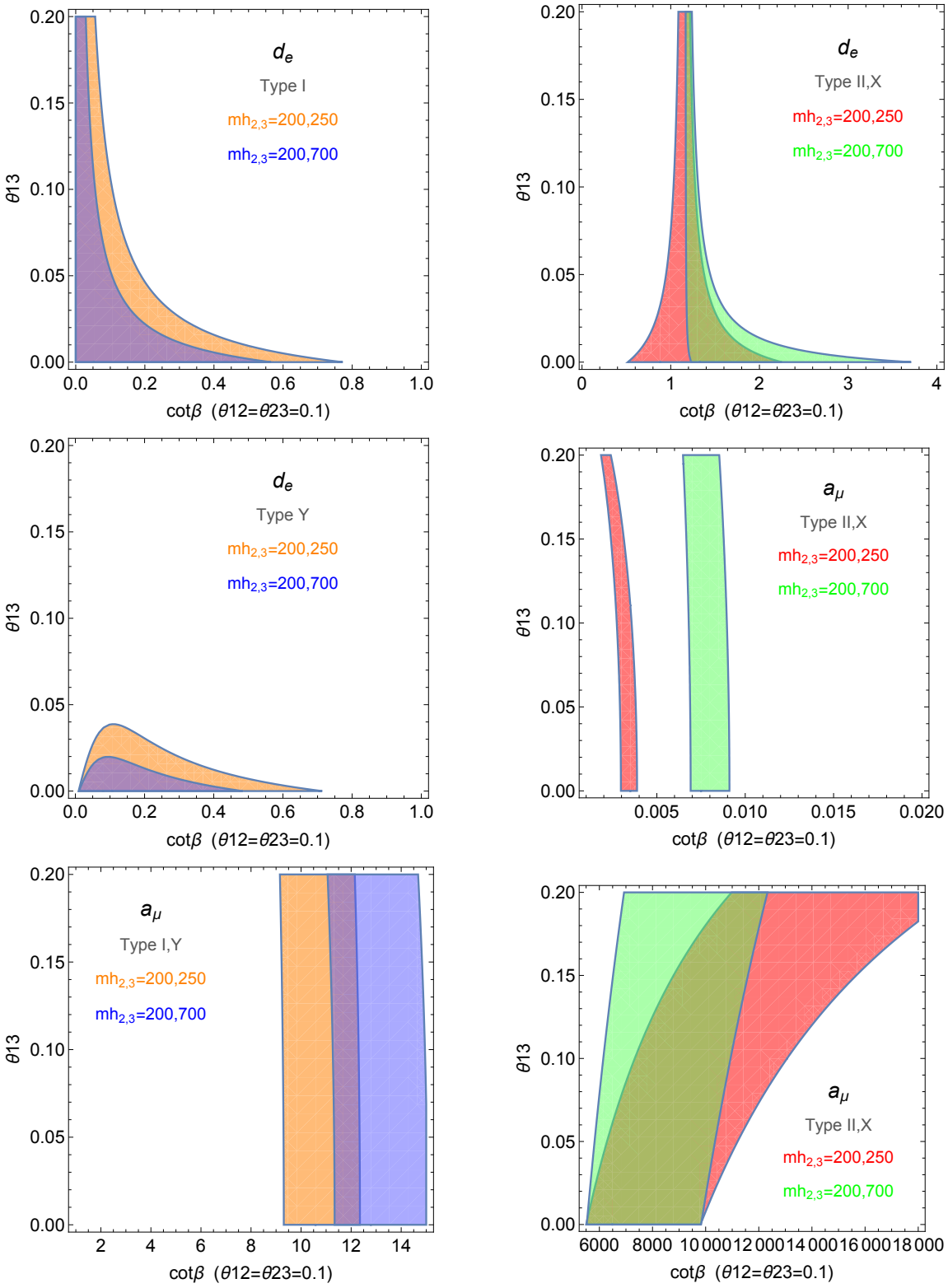

Figure 8. Regions surviving d_e bounds vs. regions producing a_μ with the deviation observed for Type I,Y (left) and Type II,X (right), for different $m_{h_{2,3}}$ masses (in GeV) and fixed values of θ_{12} and θ_{23}.

JHEP09(2018)059

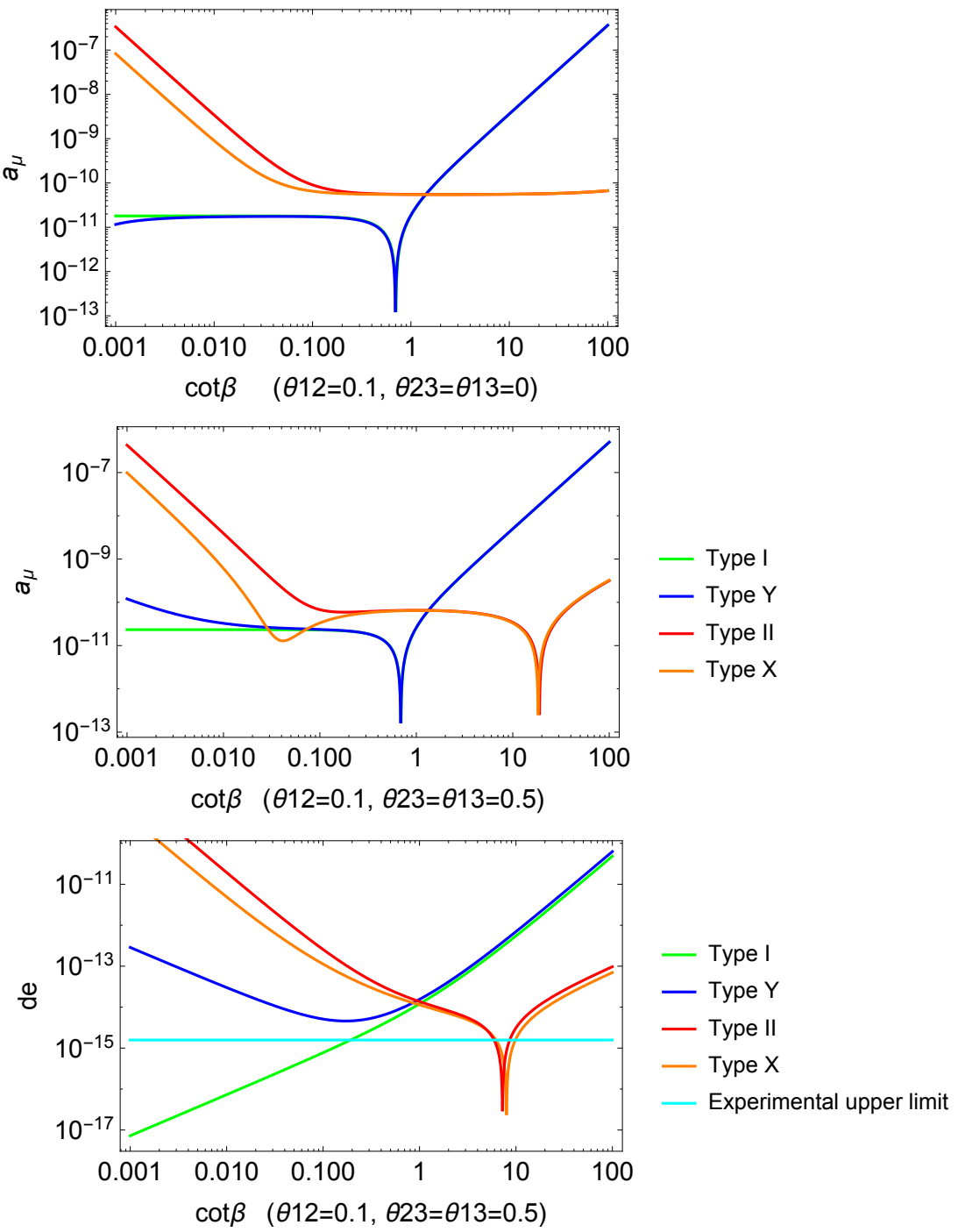

Figure 9. a_μ (top) and d_e (bottom) values in different 2HDM Types for fixed values of angles and masses ($m_{h_{2,3}} = 145, 105\,\text{GeV}$).

JHEP09(2018)059

d_e contribution increases and the surviving region of the parameter space shrinks. As mentioned before, the behaviour of Type Y and II are similar to Type I and X, respectively.

To see the effect of the scalar masses, in figure 11, we show regions producing a_μ within the 3.6σ band and regions surviving the d_e limits for mid-range scalar masses and fixed values of $\theta_{12} = \theta_{23} = 0.1$. In Type I and Y, the regions corresponding to different constraints overlap when $\cot\beta \approx 9$, and therefore in this mass range one can explain a_μ and remain compatible with the eEDM experiments. Let us stress that in Type I and Y one can satisfy the constraint on d_e at any point of the plane shown in figure 11 by changing the masses and the mass splittings. However, the region where the observed a_μ can be produced lies robustly at large $\cot\beta$, which is ruled out by too large scalar-fermion couplings. The corresponding plots for Type II and X show that in neither types there is a region where the d_e and a_μ plots overlap, with a_μ preferring the very small and very large $\cot\beta$ values while d_e bounds are satisfied in the $\cot\beta \sim \mathcal{O}(1)$.

Note that in figure 10 the value for the CP-violating angles θ_{23}, θ_{13} is chosen to be 0.5 for the a_μ plot to show the enhanced effect of CP-violation. Such a high value of CP-violation is strongly constrained by eEDMs as shown in the same figure in the d_e plot with the same θ_{23}, θ_{13} values. In figure 11 where we claim that the a_μ and d_e favourable regions overlap, the CP-violating angles are very small $\theta_{23}, \theta_{13} \simeq 0.1$ and well within the d_e bounds as shown in figure 12.

4.4.3 Light mass region

It has been shown [30, 55] that in the CP-conserving limit, Type-X 2HDM can produce a large enough a_μ due to the positive contribution from a very light CP-odd scalar, $m_A \approx 30\,\text{GeV}$, and a large $\tan\beta \approx 60$. Our calculations, when taken to the CP-conserving limit ($\theta_{13} = \theta_{23} = 0$), confirm these results.

In figure 13, we show the effect of CP-violation on the a_μ contribution in different 2HDM Types for light scalars masses. We also show the d_e contribution in different 2HDM Types in this mass region and the upper limit imposed by the eEDM experiments.

To clarify the effect of CP-violation, in figure 14, we plot a_μ and d_e contributions in Type I and X for fixed scalar mass values while varying the CP-violating angles. The corresponding plots for Type Y and II are similar to Type I and X, respectively, as discussed in detail before.

To see how different scalar masses affect the a_μ and d_e contributions, in figure 15, we show regions surviving d_e bounds and regions producing a_μ within the 3.6σ observed value in different 2HDM Types for different $m_{h_{2,3}}$ masses with fixed θ_{12}, θ_{23} values. This figure confirms our statement in figures 13: in Type I and Y, the a_μ behaviour is very similar while Type Y is more constrained by d_e data. Clearly, a_μ requires $\cot\beta \approx 10$, while d_e constrains $\cot\beta$ to be less than 1 in Type I and Y with no overlap between the two regions. Type II and X, clearly showing no overlap between the d_e and a_μ regions with a_μ preferring the very small and very large $\cot\beta$ values while d_e bounds are satisfied for $\cot\beta \sim \mathcal{O}(1)$.

Similar to the other mass regions, large $\cot\beta$ values are ruled out due to flavour and/or collider constraints in Type II and Y, and only Type I and X survive in the low $\cot\beta$ region.

JHEP09(2018)059

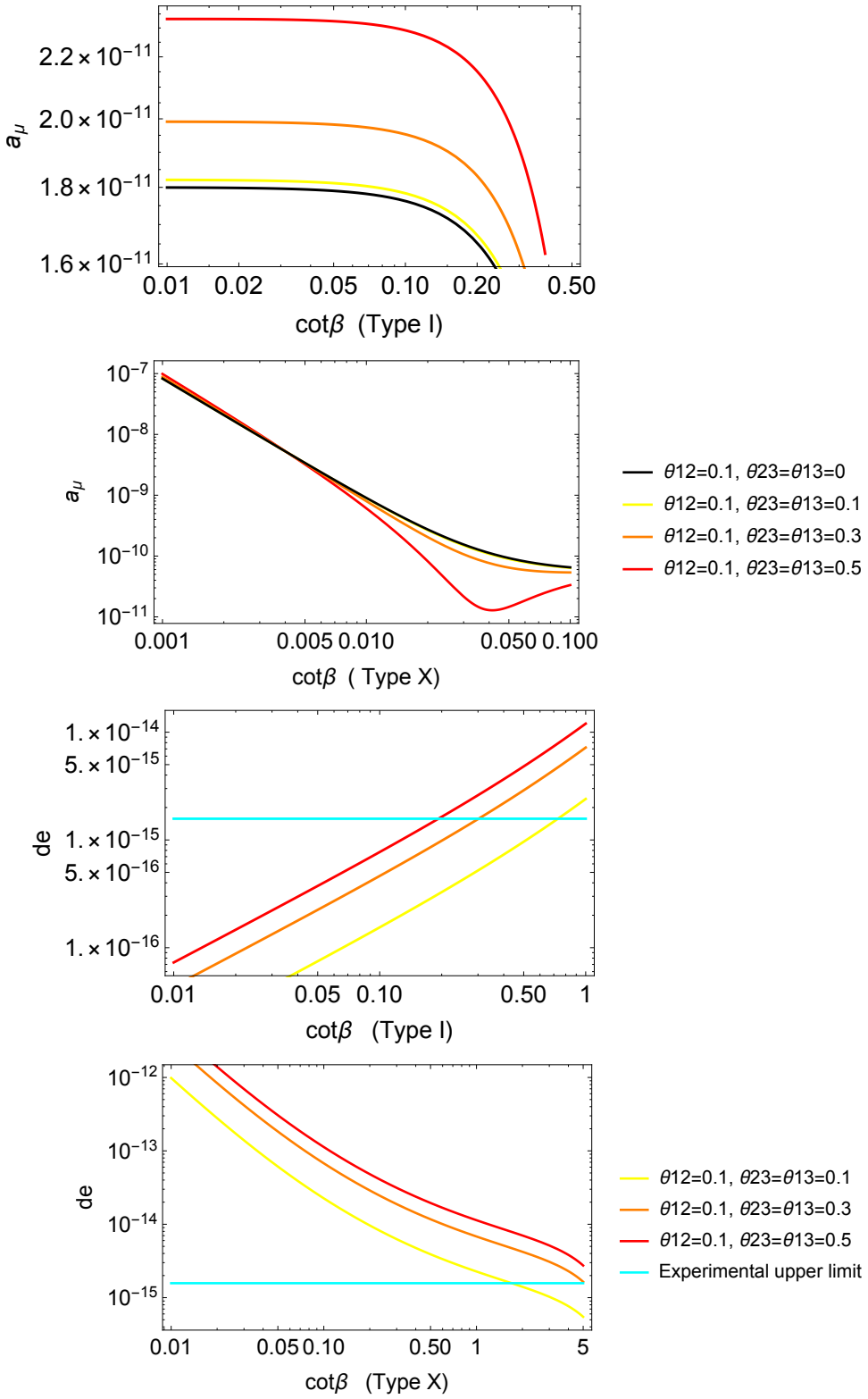

Figure 10. a_μ (top) and d_e (bottom) values in Type I and Type X for different values of angles and fixed values of masses ($m_{h_{2,3}} = 145, 105\,\text{GeV}$). The behaviour of Type Y and II are similar to Type I and X, respectively.

JHEP09(2018)059

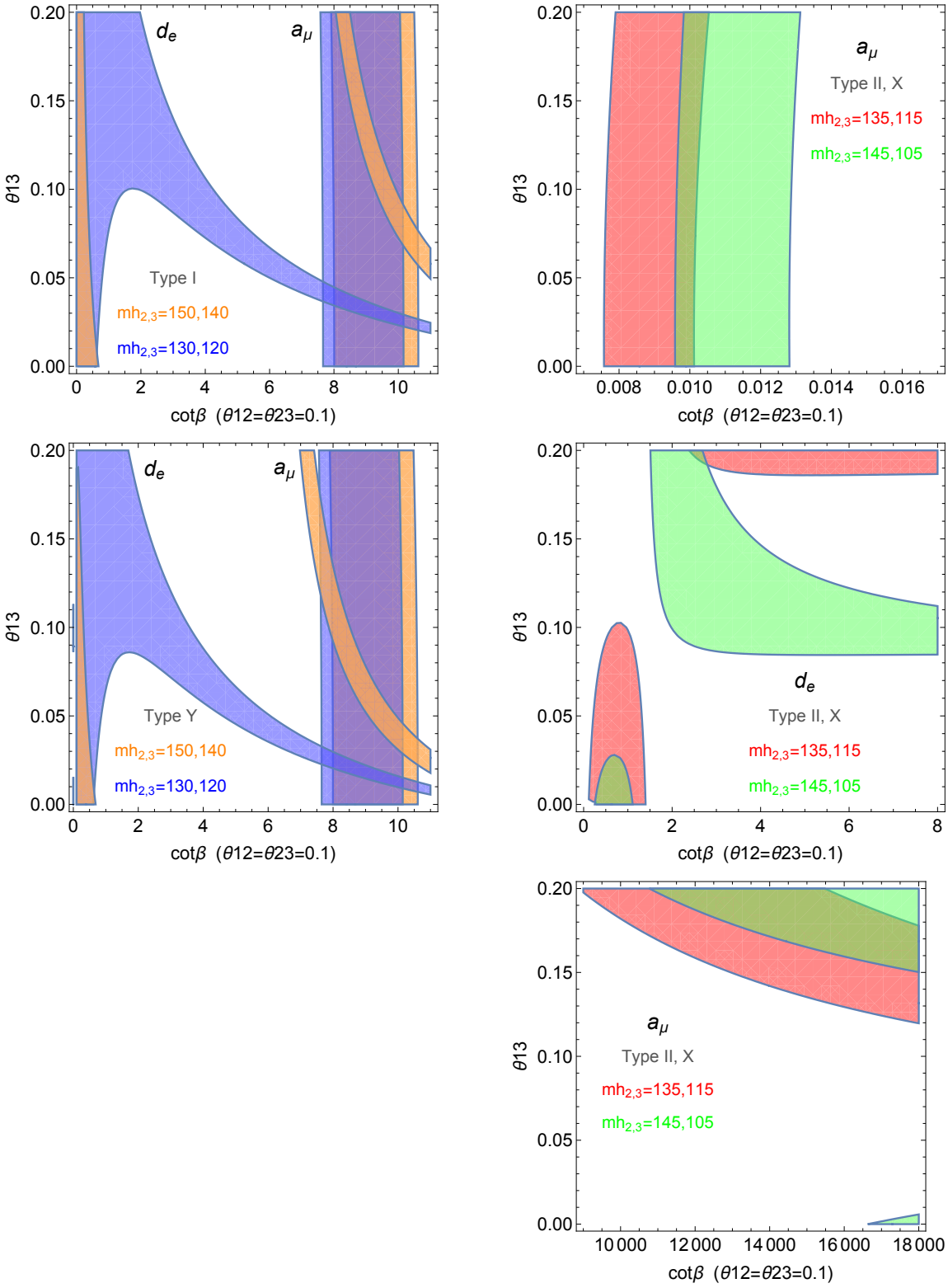

Figure 11. Regions surviving d_e bounds while producing a_μ in Type-I,Y (left) and Type II,X (right) for mid-range $m_{h_{2,3}}$ masses (in GeV) and fixed values of θ_{12} and θ_{23}. Note that in Type-I,Y plots by changing $m_{h_{2,3}}$ masses, it is possible to cover the whole plane.

JHEP09(2018)059

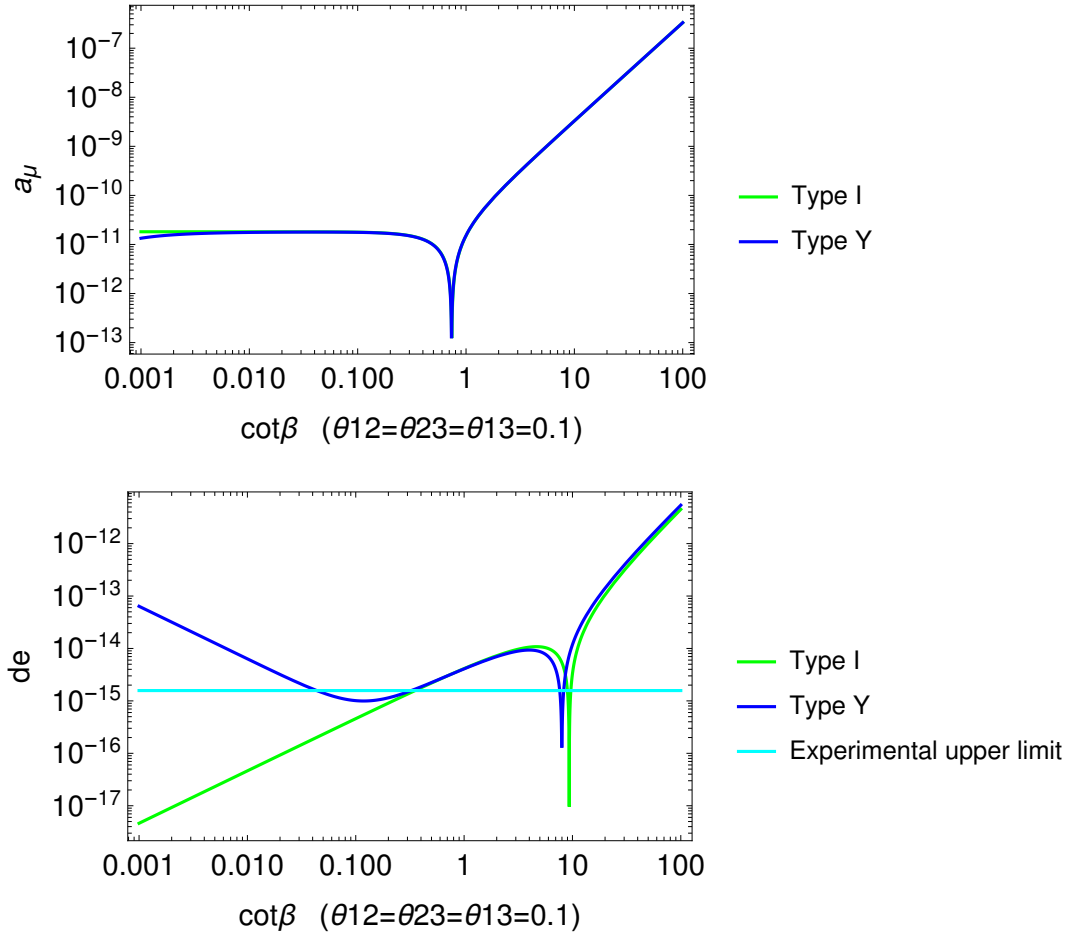

Figure 12. a_μ (top) and d_e (bottom) values in Type I,Y for fixed values of angles and masses ($m_{h_{2,3}} = 150, 140\,\text{GeV}$). Notice the d_e-surviving region $\cot\beta \approx 10$ which contributes to a_μ sufficiently.

To summarise the findings in these subsections: in all mass ranges, Type I and Y contribute efficiently to a_μ in the large $\cot\beta$ region. In Type II and X, very small $\cot\beta$ values lead to the correct a_μ values. On the other hand, bounds from d_e experiments are satisfied in the small $\cot\beta$ region for Type I and Y with Type Y more constrained, and in the $\cot\beta \gtrsim 1$ for Type II and X.

Super-imposing the d_e and a_μ plots reveal that only in Type I and Y and only in the medium mass region, one can simultaneously produce the observed contribution to a_μ and remain compatible with the results from eEDM experiments. However, this happens only at relatively large values of $\cot\beta$ ruled out by current experimental data. In the low $\cot\beta$ region we find that only Type I and Type X models remain viable: Type X is a suitable choice for obtaining a_μ contributions in the absence of CP-violation, while Type I has the smallest contribution to d_e and therefore a suitable choice for a CP-violating model, but yielding only the SM contribution to a_μ.

JHEP09(2018)059

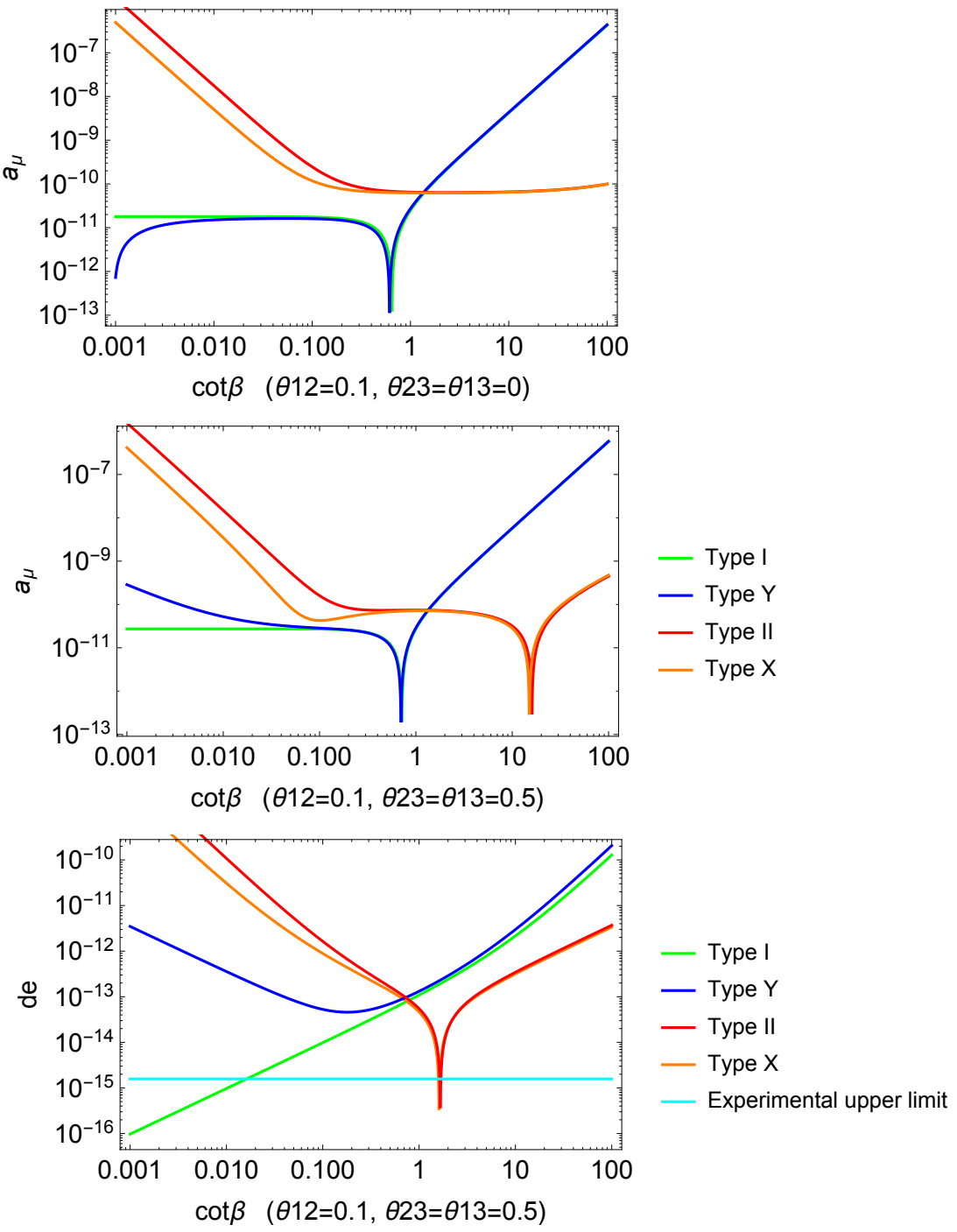

Figure 13. a_μ (top) and d_e (bottom) values in different 2HDM Types for fixed values of angles and masses ($m_{h_{2,3}} = 200, 50\,\text{GeV}$).

JHEP09(2018)059

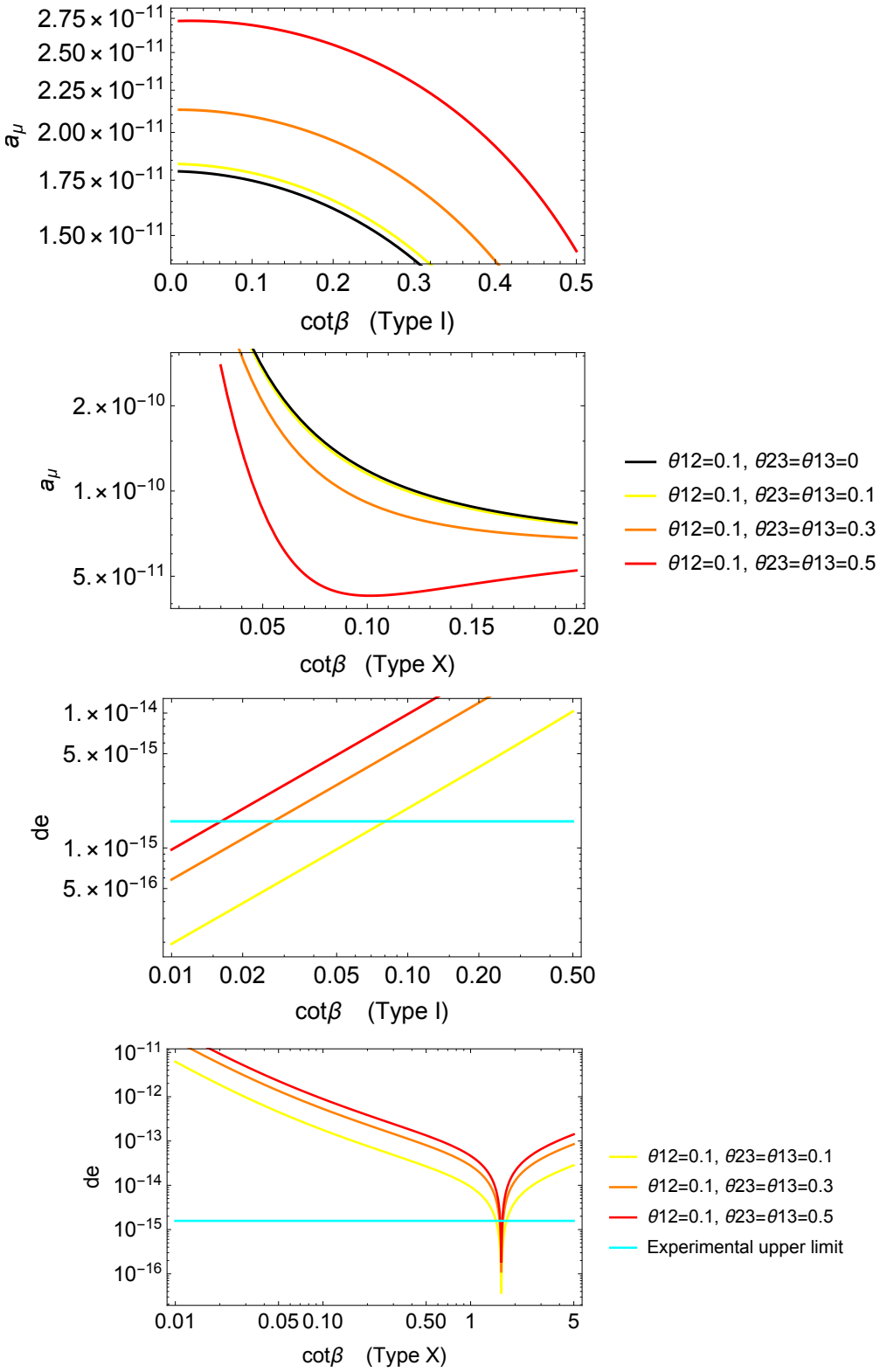

Figure 14. a_μ (top) and d_e (bottom) values in Type I (top) and Type X (bottom) for different values of angles and fixed values of masses ($m_{h_{2,3}} = 200, 50\,\text{GeV}$). The behaviour of Type Y and II are similar to Type I and X, respectively.

JHEP09(2018)059

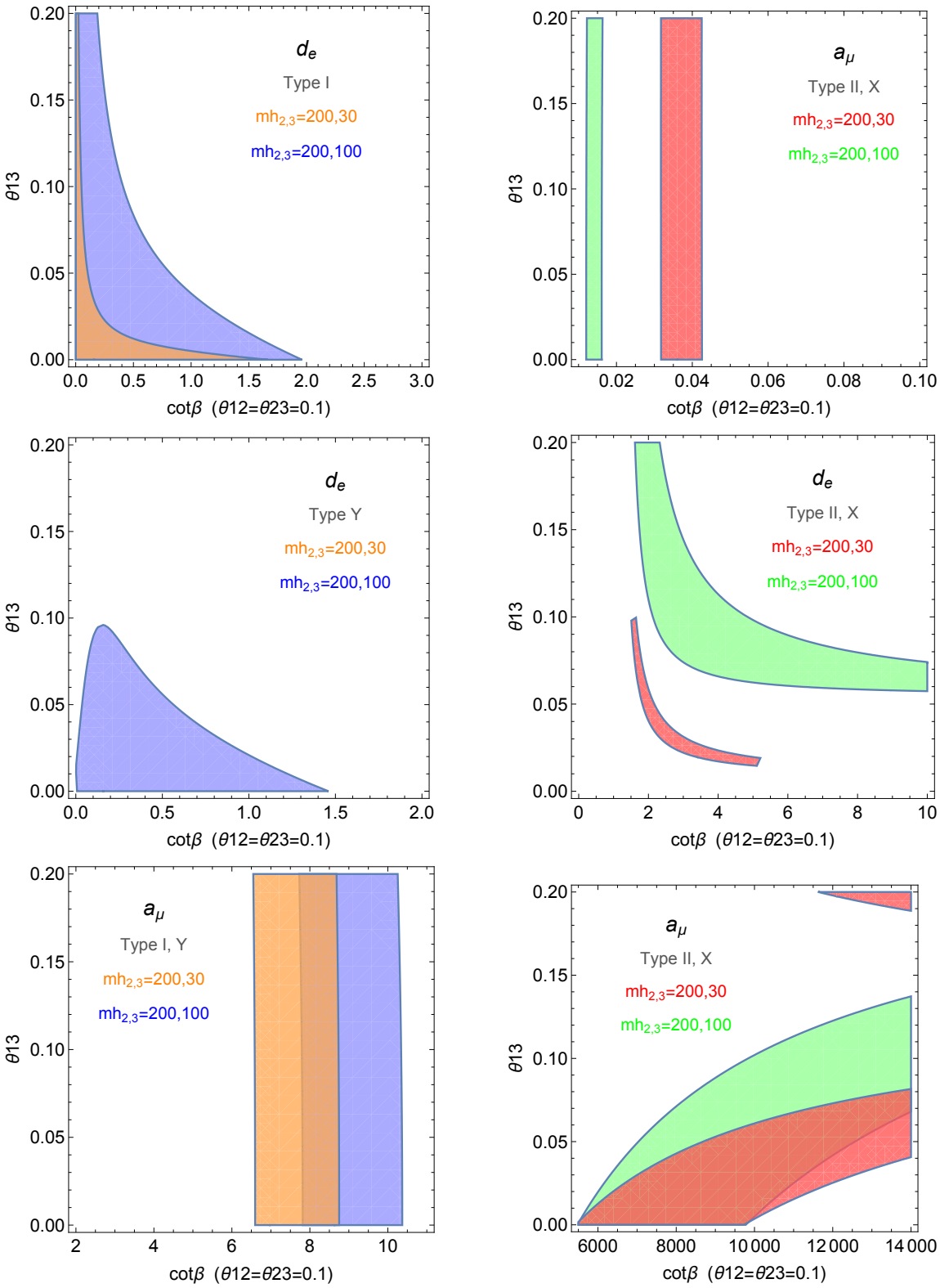

Figure 15. Regions surviving d_e bounds vs. regions producing a_μ within the deviation observed in 2HDM Type I,Y (left) and Type II,X (right) for light scalar masses (in GeV) and fixed $\theta_{12,23}$ values.

JHEP09(2018)059

5 2HDM + singlet extension

The singlet extension of the 2HDM is a relatively popular model [6, 26, 27] for several reasons: first, the scalar sector of 2HDM+S resembles that of the Next to Minimal Supersymmetric SM (NMSSM). Second, it is understood that the singlet extension of the SM and the 2HDM are incapable of providing a viable DM candidate and allow for CP-violation simultaneously [56]. Therefore, going beyond the simplest extensions of the SM seems inevitable.

In general, the decomposition of the scalar multiplets is as follows.

$$\Phi_1 = \begin{pmatrix} \phi_1^+ \\ \frac{v_1+h_1^0+ia_1^0}{\sqrt{2}} \end{pmatrix}, \quad \Phi_2 = \begin{pmatrix} \phi_2^+ \\ \frac{v_2+h_2^0+ia_2^0}{\sqrt{2}} \end{pmatrix}, \quad S = \frac{1}{\sqrt{2}}(w+\phi_4+i\phi_5). \tag{5.1}$$

Here, we discuss directly the complex singlet extension of 2HDM. The results could easily be translated to the real singlet case by setting the imaginary component of the singlet, ϕ_5, and the related parameters ($\theta_{15}, \theta_{25}, \theta_{35}, \theta_{45}$ in the rotation matrix in eq. (5.12)) to zero. Also, in the calculation of the d_e and a_μ, the sums will be over $i = 1, \ldots, 4$, corresponding to the four scalar mass eigenstates, $h_{1,2,3,4}$.

The most general 2HDM+CS potential has the form $V = V^d + V^s + V^{ds}$, where

$$\begin{aligned} V^d = &-\mu_1^2(\Phi_1^\dagger\Phi_1) - \mu_2^2(\Phi_2^\dagger\Phi_2) - \mu_3^2(\Phi_1^\dagger\Phi_2) \\ &+ \lambda_1(\Phi_1^\dagger\Phi_1)^2 + \lambda_2(\Phi_2^\dagger\Phi_2)^2 + \lambda_3(\Phi_1^\dagger\Phi_1)(\Phi_2^\dagger\Phi_2) + \lambda_4(\Phi_1^\dagger\Phi_2)(\Phi_2^\dagger\Phi_1) \\ &+ \lambda_5(\Phi_1^\dagger\Phi_2)^2 + \lambda_6(\Phi_1^\dagger\Phi_1)(\Phi_1^\dagger\Phi_2) + \lambda_7(\Phi_2^\dagger\Phi_2)(\Phi_1^\dagger\Phi_2), \end{aligned} \tag{5.2}$$

$$\begin{aligned} V_s = &-\mu_4^2(S^*S) - \mu_5^2(S^2) \\ &+ \lambda_8(S^*S)^2 + \lambda_9(S^*S)(S^2) + \lambda_{10}(S^4) \\ &+ \kappa_1(S) + \kappa_2(S^3) + \kappa_3(S)(S^*S), \end{aligned} \tag{5.3}$$

$$\begin{aligned} V_{ds} = &\lambda_{11}(\Phi_1^\dagger\Phi_1)(S^*S) + \lambda_{12}(\Phi_1^\dagger\Phi_1)(S^2) + \kappa_4(\Phi_1^\dagger\Phi_1)(S) \\ &+ \lambda_{13}(\Phi_2^\dagger\Phi_2)(S^*S) + \lambda_{14}(\Phi_2^\dagger\Phi_2)(S^2) + \kappa_5(\Phi_2^\dagger\Phi_2)(S) \\ &+ \lambda_{15}(\Phi_1^\dagger\Phi_2)(S^*S) + \lambda_{16}(\Phi_1^\dagger\Phi_2)(S^2) + \lambda_{17}(\Phi_1^\dagger\Phi_2)(S^{*2}) \\ &+ \kappa_6(\Phi_1^\dagger\Phi_2)(S) + \kappa_7(\Phi_1^\dagger\Phi_2)(S^*). \end{aligned} \tag{5.4}$$

Similarly as in the case of SM+RS, the linear term κ_1 can be removed by a translation of S.

Similar to the 2HDM, the 2HDM+CS suffers from tree-level FCNCs due to the existence of more than one scalar doublet which in general could couple to fermions. As in 2HDM, this can be alleviated by imposing a Z_2 symmetry on the scalar sector and extending it to the fermion sector in a similar manner. The transformation of the scalar multiplets under this Z_2 symmetry is fixed to be

$$\Phi_1 \to +\Phi_1, \quad \Phi_2 \to -\Phi_2, \quad S \to +S. \tag{5.5}$$

The fermionic Z_2 charges are as shown in table 1 which define the 2HDM type of the model. Imposing this symmetry on the potential while allowing for a soft breaking term

JHEP09(2018)059

μ_3^2, forbids the following parameters,

$$\lambda_6 = \lambda_7 = \lambda_{15} = \lambda_{16} = \lambda_{17} = \kappa_6 = \kappa_7 = 0. \tag{5.6}$$

CP-violation is introduced explicitly through the following complex parameters,

$$\mu_3^2,\ \mu_5^2,\ \kappa_1,\ \kappa_2,\ \kappa_3,\ \kappa_4,\ \kappa_5,\ \lambda_5, \lambda_9,\ \lambda_{10},\ \lambda_{12},\ \lambda_{14}. \tag{5.7}$$

We take the VEVs, v_1, v_2 and w to be real.

5.1 Minimisation of the 2HDM+CS potential

The minimisation conditions are presented in appendix D under which the minimum of the potential is realised at $\langle\Phi_1\rangle = v_1$, $\langle\Phi_2\rangle = v_2$, $\langle S\rangle = w$.

Similar to the 2HDM, it is useful to rotate the doublets to the Higgs basis while the singlet remains unchanged,

$$\begin{pmatrix} \widehat{\Phi}_1 \\ \widehat{\Phi}_2 \\ \widehat{S} \end{pmatrix} = \begin{pmatrix} \cos\beta & \sin\beta & 0 \\ -\sin\beta & \cos\beta & 0 \\ 0 & 0 & 1 \end{pmatrix} \begin{pmatrix} \Phi_1 \\ \Phi_2 \\ S \end{pmatrix}, \tag{5.8}$$

with $\tan\beta = v_2/v_1$. Then, only one of the doublets has a VEV,

$$\widehat{\Phi}_1 = \begin{pmatrix} G^+ \\ \frac{v+\phi_1+iG^0}{\sqrt{2}} \end{pmatrix}, \quad \widehat{\Phi}_2 = \begin{pmatrix} H^+ \\ \frac{\phi_2+i\phi_3}{\sqrt{2}} \end{pmatrix}, \quad \widehat{S} = \frac{1}{\sqrt{2}}(w + \phi_4 + i\phi_5), \tag{5.9}$$

and one can separate the Goldstone bosons, $G^\pm, G^0$, from the physical states. The charged Higgs mass is calculated to be

$$m_{H^\pm}^2 = \frac{\mathrm{Re}\mu_3^2}{\sin\beta\cos\beta} - \frac{v^2}{2}(\lambda_4 + 2\mathrm{Re}\lambda_5). \tag{5.10}$$

The neutral mass-squared matrix, $\mathcal{M}^2$, shown in detail in appendix D, is a 5×5 matrix which is diagonalised by the rotation matrix R,

$$R^T\mathcal{M}^2R = \mathcal{M}^2_{\mathrm{diag}} = \mathrm{diag}\big(m_{h_1}^2, m_{h_2}^2, m_{h_3}^2, m_{h_4}^2, m_{h_5}^2\big), \tag{5.11}$$

where, as before, we take h_1 to be the observed Higgs boson at the LHC.

The rotation matrix, R, contains ten mixing angles, $\theta_{12-15}, \theta_{23-25}$, $\theta_{34,35}$ and θ_{45} among which five represent CP-violation, namely $\theta_{13,15,23,25,34}$, and will vanish in the CP-conserving limit. We, therefore, take these angles to be small since, as it will be shown later, they prove to be very small in the interesting and allowed regions of the parameter space. Of the remaining angles θ_{12} and θ_{14} represent the mixing of the SM-like Higgs with the other CP-even states. To keep this state mostly doublet-like and to agree with the observed Higgs data, we take these angles to be small.

The remaining angles, θ_{24}, θ_{35} and θ_{45} do not contribute to the observables in which we are interested here, and therefore, to simplify the analysis, we assume all mixing angles

JHEP09(2018)059

to be small ($\cos\theta_i \simeq 1$ and $\sin\theta_i \simeq \theta_i$). As a result, the rotation matrix, R, simplifies to the form

$$\phi_i = R_{ij} h_j \; ; \qquad \begin{pmatrix} \phi_1 \\ \phi_2 \\ \phi_3 \\ \phi_4 \\ \phi_5 \end{pmatrix} = \begin{pmatrix} 1 & \theta_{12} & \theta_{13} & \theta_{14} & \theta_{15} \\ -\theta_{12} & 1 & \theta_{23} & \theta_{24} & \theta_{25} \\ -\theta_{13} & -\theta_{23} & 1 & \theta_{34} & \theta_{35} \\ -\theta_{14} & -\theta_{24} & -\theta_{34} & 1 & \theta_{45} \\ -\theta_{15} & -\theta_{25} & -\theta_{35} & -\theta_{45} & 1 \end{pmatrix} \begin{pmatrix} h_1 \\ h_2 \\ h_3 \\ h_4 \\ h_5 \end{pmatrix} . \tag{5.12}$$

With this simplified form, one can calculate the angles in terms of the parameters of the potential as shown in appendix D.

After minimisation, the 32 independent parameters of the model,

$$\mu^2_{1,2,4},\ \mathrm{Re}\mu^2_{3,5},\ \lambda_{1-4},\ \lambda_{8,11,13},\ \mathrm{Re}\kappa_{1-5},\ \mathrm{Im}\kappa_{1-5},\ \mathrm{Re}\lambda_{5,9,10,12,14},\ \mathrm{Im}\lambda_{5,9,10,12,14}, \tag{5.13}$$

can be expressed in terms of

$$\tan\beta,\ v,\ w,\ m_{h_{1-5}},\ m_{H^\pm},\ \theta_{12-15},\ \theta_{23-25},\ \theta_{34,35,45},\ \mathrm{Re}\mu^2_{3,5},\ \mathrm{Im}\kappa_{1-5},\ \mathrm{Re}\lambda_5,\ \mathrm{Im}\lambda_{5,9,10,12,14}, \tag{5.14}$$

which we take as input parameters for our numerical calculations. In all the results that follow, we take into account the same theoretical and experimental bounds as in section 4 translated to fit the 2HDM+CS model accordingly.

5.2 a_μ and d_e in 2HDM+CS

Due to the singlet nature of ϕ_4 and ϕ_5, they do not directly couple to the SM fermions and gauge bosons. As a result, the Yukawa and kinetic terms are similar to the 2HDM discussed in section 4.2 with $i = 1, \cdots, 5$, corresponding to the five scalar mass eigenstates, $h_{1,2,3,4,5}$. The last two rows of the rotation matrix in eq. (5.12) do not appear in the calculations of d_e and a_μ whose contributions are very much 2HDM-like with the sums running over all five scalar mass eigenstates, $h_{1,2,3,4,5}$, in eqs. (4.19)–(4.23).

We have studied numerically all four 2HDM-like types with an exemplary value of 0.1 for all sub-dominant angles. Similar to the 2HDM scenario, we plot the constraints on d_e and a_μ in the (θ_{13},$\cot\beta$)-plane for various values of scalar masses.

The main conclusion here is very similar to what was found in the 2HDM subsection 4.4: only in Type I and Y and only in the case of medium range masses $m_{h_{2,3,4,5}} \approx m_{h_1}$ is one able to produce the observed value of a_μ while remaining consistent with the d_e constraints as shown in figure 16. However, as mentioned before, such large values of $\cot\beta$ are ruled out due to flavour and/or collider constraints.

6 Conclusions and outlook

We have studied popular scalar extensions of the Standard Model and their contributions to the muon $(g-2)$, and electric dipole moment of the electron, eEDM. Concretely, we studied first the real and complex singlet extension of the SM, and second, as the main

JHEP09(2018)059

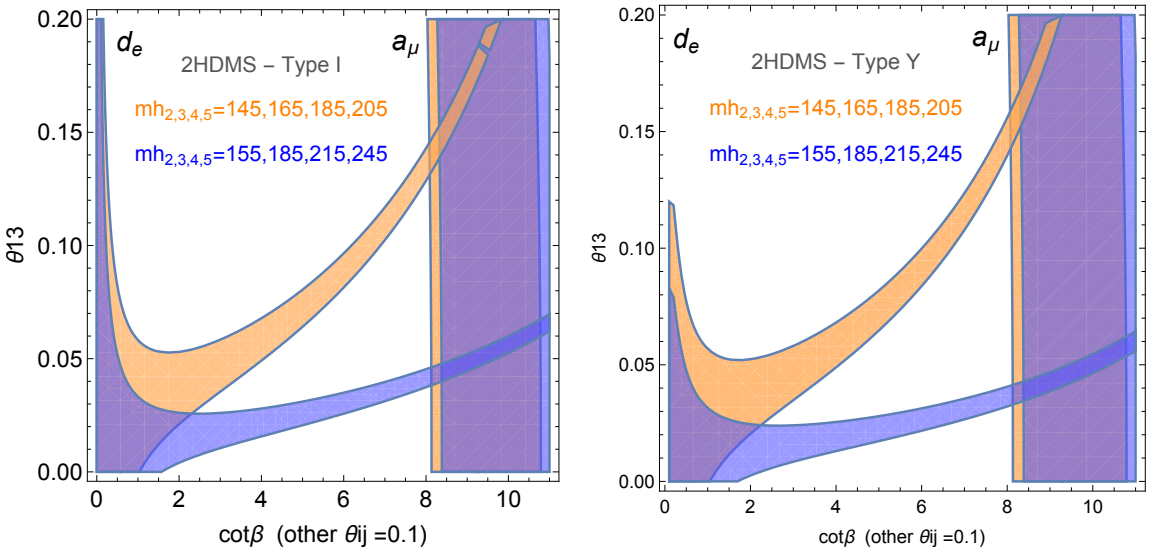

Figure 16. Regions surviving d_e bounds while producing a_μ in 2HDM+CS Type-I and Y for mid-range $m_{h_{2,3,4,5}}$ masses (in GeV) and fixed values of angles. Note that by changing $m_{h_{2,3,4,5}}$ masses, it is possible to cover the whole plane.

part of our analysis, we considered the 2-Higgs doublet model (2HDM) of Types I, II, X and Y and the 2HDM extended with the inclusion of a singlet scalar.

In the singlet extension of the SM, CP-violation is introduced by a non-trivial higher dimensional operator connecting the singlet scalar with the Higgs field and the top quark. We found that while the imaginary part of this coupling can be compatible with the eEDM bounds, a very large real part must be introduced in order to explain a_μ.

In the CP-conserving limit, extensive $(g-2)_\mu$ studies have been done in different types of 2HDM with varying scalar masses, mixing angles and $\tan\beta$s in the literature. It has been shown that at 1-loop level contributions to a_μ are positive for the CP-even scalars and negative for the CP-odd scalars (and the charged scalar whose negative effect is negligible). The dominant contribution is from the 2-loop processes to which CP-even scalars contribute negatively and CP-odd scalars contribute possitively. As a result, very light CP-odd scalars have been shown to produce a large enough a_μ in large $\tan\beta$ regions for Type II,X and large $\cot\beta$ regons in Type I,Y. It is, therefore, intuitive to expect that by introducing CP-violation, less dramatic values of $\tan\beta/\cot\beta$ or scalar masses are required to produce an adequate a_μ contribution.

All our calculations, confirm the known results in the CP-conserving limit and show the well-understood $(g-2)_\mu$ behaviour of different 2HDM types for varying masses in a wide range of $\tan\beta$s. Incremental changes in the scalar masses do not change the a_μ drastically. By introducing CP-violation, which only adds the two CP-violating angles θ_{13} and θ_{23} to the known input parameters, we show that indeed the value of a_μ is affected. This effect, however small, is enhanced by increasing the amount of CP-violation (manifested in the values of θ_{13}, θ_{23} angles). On the other hand, θ_{13}, θ_{23} angles are strongly constrained by eEDM experiments which only leave a small window in the parameter space to be explored.

JHEP09(2018)059

We provide the detailed formulas for a_μ and d_e contributions to show the subdominant effect of the parameters for which an exemplary value has been chosen in the plots.

In particular, we found that only when all scalars are relatively close in mass, CP-violating Type I and Y 2HDMs explain the muon anomalous magnetic moment in $\cot\beta \sim 10$ which is also allowed by the eEDM constraints. However, such large values of $\cot\beta$ are already ruled out by flavour/collider experiments. Therefore, given the current status of the global set of constraints applied on all values of $\cot\beta$, in the CP-violating 2HDM, there exist no viable parameter space in agreement with both a_μ and eEDM bounds. In the low $\cot\beta$ region, Type X remains the only 2HDM type which has a large enough contribution to a_μ, while Type I is the preferred type when introducing CP-violation as it contributes minimally to d_e.

In the singlet extension of the 2HDM, we show that the 2HDM behaviour is repeated and the model is capable of explaining the $(g-2)_\mu$ within the d_e bounds when all scalars are relatively close in mass and the Yukawa interactions are of Type I and Y. However, this only occurs in the $\cot\beta \approx 10$ region which, again, is ruled out by flavour and collider experiments.

We have presented a robust way to implement the constraints on the muon anomalous magnetic moment and electric dipole moment of the electron on these models. Our central finding is that this allows one to categorically exclude different types of 2HDMs and 2HDM+CS and, consequently, identify most viable Yukawa interaction patterns which would be useful for more general model building based e.g. on the paradigm of minimal flavour violation.

The scalar extensions we have studied are applied in attempts to explain the BAU via electroweak baryogenesis. Since then also CP violation in the new sector needs to be introduced, our results help in establishing phenomenological viability of these models.

Acknowledgments

The authors would like to thank Dominik Stoeckinger for useful discussions. We acknowledge support from the Academy of Finland projects 274503, 267842 and 310130. VK also acknowledges support from the H2020-MSCA-RISE-2014 grant no. 645722 (NonMinimalHiggs). NK is supported by Vilho, Yrjö and Kalle Väisälä Foundation.

A Loop functions

The loop functions are:

$$f(z) = \frac{1}{2} z \int_0^1 dx \frac{1-2x(1-x)}{x(1-x)-z} \log\left(\frac{x(1-x)}{z}\right), \tag{A.1}$$

$$g(z) = \frac{1}{2} z \int_0^1 dx \frac{1}{x(1-x)-z} \log\left(\frac{x(1-x)}{z}\right), \tag{A.2}$$

$$h(z) = z^2 \frac{\partial}{\partial z}\left(\frac{g(z)}{z}\right) = \frac{z}{2}\int_0^1 \frac{dx}{z-x(1-x)}\left[1 + \frac{z}{z-x(1-x)} \log\left(\frac{x(1-x)}{z}\right)\right]. \tag{A.3}$$

JHEP09(2018)059

B Details of minimisation of the 2HDM potential

The elements of the symmetric neutral mass-squared matrix, $\mathcal{M}^2$ in eq. (4.9), are of the form

$$\begin{aligned}
\mathcal{M}^2_{11} &= \frac{1}{8}v^2\Big(4\cos(2\beta)(\lambda_1-\lambda_2)+\lambda_1\cos(4\beta)+\lambda_2\cos(4\beta)-\lambda_3\cos(4\beta)-\lambda_4\cos(4\beta)\\
&\qquad +3\lambda_1+3\lambda_2+\lambda_3+\lambda_4+4\sin^2(2\beta)\mathrm{Re}\lambda_5\Big)\\
\mathcal{M}^2_{12} &= -\frac{1}{4}v^2\sin(2\beta)\left[\cos(2\beta)\lambda_{1234}+\lambda_1-\lambda_2-2\cos(2\beta)\mathrm{Re}\lambda_5\right]\\
\mathcal{M}^2_{13} &= -v^2\sin(\beta)\cos(\beta)\mathrm{Im}(\lambda_5)\\
\mathcal{M}^2_{22} &= \frac{1}{4}\left[2\csc(\beta)\sec(\beta)\mathrm{Re}\mu_3^2+v^2\sin^2(2\beta)(\lambda_{1234}-2\mathrm{Re}\lambda_5)\right]\\
\mathcal{M}^2_{23} &= -\frac{1}{2}v^2\cos(2\beta)\mathrm{Im}(\lambda_5)\\
\mathcal{M}^2_{33} &= \csc(2\beta)\mathrm{Re}\mu_3^2-v^2\mathrm{Re}\lambda_5,
\end{aligned} \tag{B.1}$$

where $\lambda_{1234}=\lambda_1+\lambda_2-\lambda_3-\lambda_4$.

The angles defining the rotation matrix, R in eq. (4.10), are calculated to be

$$\theta_{12} = \frac{v^2(2\sin(2\beta)(\lambda_1-\lambda_2)+\sin(4\beta)(\lambda_{1234}-2\mathrm{Re}\lambda_5))}{\rho_2-4\csc(\beta)\sec(\beta)\mathrm{Re}\mu_3^2} \tag{B.2}$$

$$\theta_{13} = \frac{8v^2\sin^2(2\beta)\mathrm{Im}(\lambda_5)(\cos(2\beta)(\lambda_1-\lambda_2)+\lambda_{1234}+2\mathrm{Re}\lambda_5)}{\rho_3-2v^2\sin(2\beta)\left[\rho_4+\rho_5-4(\cos(4\beta)+7)\mathrm{Re}\lambda_5^2\right]} \tag{B.3}$$

$$\theta_{23} = \frac{2\mathrm{Im}(\lambda_5)\left[\rho_6-16\cos(2\beta)\mathrm{Re}\mu_3^2\right]}{\rho_3-2v^2\sin(2\beta)\left[\rho_4+\rho_5-4(\cos(4\beta)+7)\mathrm{Re}\lambda_5^2\right]}, \tag{B.4}$$

where

$$\rho_1 = \cos(2\beta)(\lambda_1-\lambda_2) \tag{B.5}$$

$$\rho_2 = 2v^2\left[2\rho_1+\lambda_1+\lambda_2+\lambda_3+\lambda_4+\cos(4\beta)(\lambda_{1234}-2\mathrm{Re}\lambda_5)+2\mathrm{Re}\lambda_5\right] \tag{B.6}$$

$$\rho_3 = 8\mathrm{Re}\mu_3^2\left[(\cos(4\beta)-1)\lambda_{1234}-2(\cos(4\beta)+3)\mathrm{Re}\lambda_5\right] \tag{B.7}$$

$$\rho_4 = (\cos(4\beta)-1)\left(4\lambda_1\lambda_2-(\lambda_3+\lambda_4)^2\right) \tag{B.8}$$

$$\rho_5 = -4\mathrm{Re}\lambda_5\left[4\rho_1+\cos(4\beta)(\lambda_3+\lambda_4)+4\lambda_1+4\lambda_2-\lambda_3-\lambda_4\right] \tag{B.9}$$

$$\rho_6 = 2v^2\sin(2\beta)\left[4\cos(2\beta)(\lambda_1+\lambda_2)+(\cos(4\beta)+3)(\lambda_1-\lambda_2)+8\cos(2\beta)\mathrm{Re}\lambda_5\right]. \tag{B.10}$$

C Constraints on the parameters

C.1 Theoretical bounds

1. **Stability of the potential.** The scalar potential stability requires the potential to be bounded from below in any direction of the scalar space whose necessary and sufficient conditions are [57]

$$\lambda_1>0,\quad \lambda_2>0,\quad \sqrt{\lambda_1\lambda_2}+\lambda_3+\mathrm{MIN}(0,\ \lambda_4-|\lambda_5|)>0. \tag{C.1}$$

JHEP09(2018)059

2. **Positive-definiteness of the Hessian-positivity of mass eigenvalues.** For the point $\langle\Phi_1\rangle = \frac{v_1}{\sqrt{2}}$, $\langle\Phi_2\rangle = \frac{v_2}{\sqrt{2}}$ to be a minimum of the potential, the second order derivative matrix must have a positive definite determinant.

   Similar constrains are achieved by requiring the mass eigenvalues to be positive.

3. **Perturbative unitarity.** S-matrix unitarity for 2 to 2 elastic scattering, constrains the value of combinations of λs in the potential [58, 59].

4. **Electroweak precision data.** Extra scalars affect the gauge boson propagators, parametrized by the oblique parameters S, T, U [60]–[61] by contributing to the neutral and charged current processes at low energies (T), or to neutral current processes at different energy scales (S). U is generally small in new physics models. These parameters are constrained to be

$$S = 0.05 \pm 0.11, \quad T = 0.09 \pm 0.13, \quad U = 0.01 \pm 0.11, \tag{C.2}$$

   determined from a fit with reference mass values of top and Higgs boson $m_t = 173\,\text{GeV}$ and $m_h = 125\,\text{GeV}$ are [62, 63].

C.2 Experimental bounds

1. **Flavour constraints.** The B physics data provides constraints on $m_{H^\pm}$ and $\tan\beta$ in 2HDMs [64–67]. Ref. [52] provides a comprehensive study on various B physics observables such as $b \to s\gamma$, B^0-$\bar{B}^0$ mixing, $B \to \tau\nu$ in 2HDMs.

   Recently, the BaBar Collaboration has reported a measured ratios $\text{BR}(B \to D^*\tau\nu)/\text{BR}(B \to D^*\ell\nu)$ and $\text{BR}(B \to D\tau\nu)/\text{BR}(B \to D\ell\nu)$ ($\ell = e, \mu$) to deviate from the SM predictions by 2.7 σ and 2.0 σ, respectively, and their combined deviation is 3.4 σ [68]. Note that these deviations cannot be simultaneously explained by a Z_2 symmetric 2HDM which is flavour conserving, with or withour CP-violation.

2. **Direct searches for extra Higgs bosons at the LHC.** The search for extra neutral Higgs bosons decaying into bb, $\tau\tau$, $\gamma\gamma$, $Z\gamma$, ZZ, WW, hh and hZ [69–108] using the LHC Run-I and II data, excludes $\tan\beta \gtrsim 10$ (30) for $m_A = 300$ (700) GeV in MSSM. A similar bound is expected in the non-supersymmetric Type-II 2HDM, since the structure of the Yukawa interactions are the same. In Type-I 2HDM, there is no $\tan\beta$ enhancement in the Yukawa couplings since the Yukawa couplings are suppressed by the factor of $\cot\beta$. The production cross section is, therefore, suppressed by $\cot^2\beta$.

3. ***A → Zh* searches.** Using LHC Run-I data, an upper limit on the $\sigma(gg \to A) \times \text{BR}(A \to Zh) \times \text{BR}(h \to f\bar{f})$ has been given [74] for $m_A = 220\text{-}1000\,\text{GeV}$. The upper limit for $f = \tau\,(b)$ is measured to be $0.098 - 0.013$ pb ($0.57 - 0.014$ pb). Our typical $gg \to H, A$ cross section is $\simeq 1$ pb for $m_{H,A} = 200\,\text{GeV}$ and $\tan\beta \gtrsim 2$, and the $A \to Zh$ branching ratio is $\lesssim 10^{-2}$. Considering that the decay rate of the SM-like Higgs boson does not change much from the SM prediction, the $h \to \tau\tau(b\bar{b})$ branching ratio is $\sim 7\%(60\%)$, meaning that our cross section is well below the upper limit.

JHEP09(2018)059

4. **Gauge bosons width.** The contribution of the extra scalars to the total gauge bosons widths [109] constrain the scalar masses:

$$m_{H,A} + m_{H^\pm} \geq m_W, \;\; m_H + m_A \geq m_Z, \;\; 2\, m_{H^\pm} \geq m_Z. \tag{C.3}$$

5. **Direct searches for charged scalars and their lifetime.** A conservative lower limit for the mass of charged scalars is taken to be: $m_{H^\pm} \geq 70\,\text{GeV}$ [110–117].

   Moreover, to satisfy the bounds from long-lived charged particle searches, an upper limit is set on their lifetime to be $\tau_{H^\pm} \leq 10^{-7}\,\text{s}$, to guarantee their decay within the detector, which translates to an upper bound on their total decay width $\Gamma^{\text{tot}}_{H^\pm} \geq 6.58 \times 10^{-18}\,\text{GeV}$.

6. **Higgs signal strength.** The signal strength, μ_{XY}, of the SM-like Higgs boson h_1 [98, 118–128], defined as

$$\begin{aligned} \mu_{XY} &= \frac{\sigma(gg \to h_1)}{\sigma(gg \to h_{\text{SM}})} \times \frac{\text{BR}(h_1 \to XY)}{\text{BR}(h_{\text{SM}} \to XY)}, \quad XY = W^+W^-,\; ZZ,\; gg,\; \gamma\gamma,\; Z\gamma,\; \tau^+\tau^-, \\ \mu_{b\bar{b}} &= \frac{\sigma(q\bar{q} \to h_1 V)}{\sigma(q\bar{q} \to h_{\text{SM}} V)} \times \frac{\text{BR}(H_1 \to b\bar{b})}{\text{BR}(h_{\text{SM}} \to b\bar{b})}. \end{aligned} \tag{C.4}$$

   limits the contribution from new scalars to the Higgs observables.

D Details of minimisation of the 2HDM+CS potential

The minimum of the potential is realised at

$$\begin{aligned} \mu_1^2 &= \frac{1}{8}\Big(-8t_\beta \text{Re}\mu_3^2 - 2v^2 c_{3\beta} c_\beta^{-1} \text{Re}\lambda_5 + 2v^2 \text{Re}\lambda_5 + 8w^2 \text{Re}\lambda_{12} + 8\sqrt{2} w \text{Re}\kappa_4 \\ &\quad + 2\lambda_1 v^2 c_{3\beta} c_\beta^{-1} - \lambda_3 v^2 c_{3\beta} c_\beta^{-1} - \lambda_4 v^2 c_{3\beta} c_\beta^{-1} + 6\lambda_1 v^2 + \lambda_3 v^2 + \lambda_4 v^2 + 4\lambda_{11} w^2\Big) \\ \mu_2^2 &= \frac{1}{8}\Big(-8t_\beta^{-1} \text{Re}\mu_3^2 + 2v^2 s_{3\beta} s_\beta^{-1} \text{Re}\lambda_5 + 2v^2 \text{Re}\lambda_5 + 8w^2 \text{Re}\lambda_{14} + 8\sqrt{2} w \text{Re}\kappa_5 \\ &\quad - 2\lambda_2 v^2 s_{3\beta} s_\beta^{-1} + \lambda_3 v^2 s_{3\beta} s_\beta^{-1} + \lambda_4 v^2 s_{3\beta} s_\beta^{-1} + 6\lambda_2 v^2 + \lambda_3 v^2 + \lambda_4 v^2 + 4\lambda_{13} w^2\Big) \\ \text{Im}\mu_3^2 &= v^2 s_\beta c_\beta \text{Im}\lambda_5 \\ \mu_4^2 &= \frac{1}{2w}\Big(2\sqrt{2}\text{Re}\kappa_1 + \sqrt{2} v^2 c_\beta^2 \text{Re}\kappa_4 + \sqrt{2} v^2 c s_\beta^2 \text{Re}\kappa_5 + 2v^2 w c_\beta^2 \text{Re}\lambda_{12} \\ &\quad + 2v^2 w s_\beta^2 \text{Re}\lambda_{14} + 4w^3 \text{Re}\lambda_{10} + 4w^3 \text{Re}\lambda_9 + 3\sqrt{2} w^2 \text{Re}\kappa_2 \\ &\quad + 3\sqrt{2} w^2 \text{Re}\kappa_3 - 4w \text{Re}\mu_5^2 + \lambda_{11} v^2 w c_\beta^2 + \lambda_{13} v^2 w s_\beta^2 + 2\lambda_8 w^3\Big) \\ \text{Im}\mu_5^2 &= \frac{1}{4w}\Big(2\sqrt{2}\text{Im}\kappa_1 + \sqrt{2} v^2 c_\beta^2 \text{Im}\kappa_4 + \sqrt{2} v^2 s_\beta^2 \text{Im}\kappa_5 + 2v^2 w c_\beta^2 \text{Im}\lambda_{12} \\ &\quad + 2v^2 w s_\beta^2 \text{Im}\lambda_{14} + 4w^3 \text{Im}\lambda_{10} + 2w^3 \text{Im}\lambda_9 + 3\sqrt{2} w^2 \text{Im}\kappa_2 + \sqrt{2} w^2 \text{Im}\kappa_3\Big). \end{aligned} \tag{D.1}$$

JHEP09(2018)059

The elements of the symmetric neutral mass-squared matrix, $\mathcal{M}^2$ in eq. (5.11), are of the form

$$
\begin{aligned}
\mathcal{M}^2_{11} &= \frac{1}{8}v^2(4\cos(2\beta)(\lambda_1-\lambda_2)+3\lambda_1+3\lambda_2+\lambda_3+\lambda_4+\cos(4\beta)(\lambda_{1234}-2\mathrm{Re}\lambda_5)+2\mathrm{Re}\lambda_5)\\
\mathcal{M}^2_{12} &= -\frac{1}{4}v^2\sin(2\beta)(\cos(2\beta)\lambda_{1234}+\lambda_1-\lambda_2-2\cos(2\beta)\mathrm{Re}\lambda_5)\\
\mathcal{M}^2_{13} &= -v^2\sin(\beta)\cos(\beta)\mathrm{Im}(\lambda_5)\\
\mathcal{M}^2_{14} &= \frac{1}{2}v\left(\cos^2(\beta)\left(\sqrt{2}\mathrm{Re}\kappa_4+2w\mathrm{Re}\lambda_{12}+\lambda_{11}w\right)+\sin^2(\beta)\left(\sqrt{2}\mathrm{Re}\kappa_5+2w\mathrm{Re}\lambda_{14}+\lambda_{13}w\right)\right)\\
\mathcal{M}^2_{15} &= -\frac{1}{2}v\left(\cos^2(\beta)\left(\sqrt{2}\mathrm{Im}(\kappa_4)+2w\mathrm{Im}(\lambda_{12})\right)+\sin^2(\beta)\left(\sqrt{2}\mathrm{Im}(\kappa_5)+2w\mathrm{Im}(\lambda_{14})\right)\right)\\
\mathcal{M}^2_{22} &= \frac{1}{4}\left(2\csc(\beta)\sec(\beta)\mathrm{Re}\mu_3^2+v^2\sin^2(2\beta)(\lambda_{1234}-2\mathrm{Re}\lambda_5)\right)\\
\mathcal{M}^2_{23} &= -\frac{1}{2}v^2\cos(2\beta)\mathrm{Im}(\lambda_5)\\
\mathcal{M}^2_{24} &= -\frac{1}{4}v\sin(2\beta)\left(\sqrt{2}\mathrm{Re}\kappa_4-\sqrt{2}\mathrm{Re}\kappa_5+w(\lambda_{11}-\lambda_{13}+2\mathrm{Re}\lambda_{12}-2\mathrm{Re}\lambda_{14})\right)\\
\mathcal{M}^2_{25} &= \frac{1}{4}v\sin(2\beta)\left(\sqrt{2}\mathrm{Im}(\kappa_4)-\sqrt{2}\mathrm{Im}(\kappa_5)+2w(\mathrm{Im}(\lambda_{12})-\mathrm{Im}(\lambda_{14}))\right)\\
\mathcal{M}^2_{33} &= \csc(2\beta)\mathrm{Re}\mu_3^2-v^2\mathrm{Re}\lambda_5\\
\mathcal{M}^2_{34} &= 0\\
\mathcal{M}^2_{35} &= 0\\
\mathcal{M}^2_{44} &= \frac{1}{4w}\Big(-2\sqrt{2}\mathrm{Re}(\kappa_1)-\sqrt{2}v^2\cos^2(\beta)\mathrm{Re}\kappa_4-\sqrt{2}v^2\sin^2(\beta)\mathrm{Re}\kappa_5\\
&\qquad +8w^3\mathrm{Re}\lambda_{10}+8w^3\mathrm{Re}\lambda_9+3\sqrt{2}w^2\mathrm{Re}\kappa_2+3\sqrt{2}w^2\mathrm{Re}\kappa_3+4\lambda_8w^3\Big)\\
\mathcal{M}^2_{45} &= \frac{1}{4w}\Big(2\sqrt{2}\mathrm{Im}(\kappa_1)+\sqrt{2}v^2\cos^2(\beta)\mathrm{Im}(\kappa_4)+\sqrt{2}v^2\sin^2(\beta)\mathrm{Im}(\kappa_5)-8w^3\mathrm{Im}(\lambda_{10})\\
&\qquad -4w^3\mathrm{Im}(\lambda_9)-3\sqrt{2}w^2\mathrm{Im}(\kappa_2)-\sqrt{2}w^2\mathrm{Im}(\kappa_3)\Big)\\
\mathcal{M}^2_{55} &= -\frac{1}{4w}\Big(2\sqrt{2}\mathrm{Re}(\kappa_1)+\sqrt{2}v^2\cos^2(\beta)\mathrm{Re}\kappa_4+\sqrt{2}v^2\sin^2(\beta)\mathrm{Re}\kappa_5\\
&\qquad +4v^2w\cos^2(\beta)\mathrm{Re}\lambda_{12}+4v^2w\sin^2(\beta)\mathrm{Re}\lambda_{14}+16w^3\mathrm{Re}\lambda_{10}\\
&\qquad +4w^3\mathrm{Re}\lambda_9+9\sqrt{2}w^2\mathrm{Re}\kappa_2+\sqrt{2}w^2\mathrm{Re}\kappa_3-8w\mathrm{Re}\mu_5^2\Big).
\end{aligned}
\tag{D.2}
$$

The zero entries in the mass-squared matrix are the result of the imposed Z_2 symmetry and vanishing parameters in eq. (5.6).

The angles defining the rotation matrix, R in eq. (5.12), can be calculated in the general case, however the expressions are too lengthy to present here. We only show the values of the angles in the following approximation

$$
\mathrm{Im}\kappa_{1-5} = \mathrm{Re}\kappa_{1-5} = \mathrm{Im}\lambda_{5,9,10,12,14} = \mathrm{Re}\lambda_{5,9,10,12,14} = \lambda_{11,13} = \epsilon \ll 1, \tag{D.3}
$$

JHEP09(2018)059

which is obtained by assuming that CP-violation is small and h_1 is mostly CP-even and doublet-like. As a result, the angles are calculated to be as follows.

$$
\begin{aligned}
\theta_{12} &= \frac{v^2 \sin(2\beta)(\cos(2\beta)(\lambda_{1234}-2\epsilon)+\lambda_1-\lambda_2)}{v^2(\cos(4\beta)(\lambda_{1234})+2\cos(2\beta)(\lambda_1-\lambda_2)+\lambda_1+\lambda_2+\lambda_3+\lambda_4)-2\csc(\beta)\sec(\beta)\mathrm{Re}\mu_3^2}\\
\theta_{13} &= \frac{2v^2\epsilon(\cos(2\beta)(\lambda_1-\lambda_2)+\lambda_{1234})}{v^2\sin(2\beta)\left(4\lambda_1\lambda_2-(\lambda_3+\lambda_4)^2\right)-4\mathrm{Re}\mu_3^2(\lambda_{1234})}\\
\theta_{14} &= \frac{v\left(3w+\sqrt{2}\right)\epsilon\left(16\mathrm{Re}\mu_3^2-2\sin(2\beta)\left(v^2\cos(4\beta)(\lambda_{1234})+v^2(-\lambda_{1234})+8\lambda_8 w^2\right)\right)}{\sin(2\beta)\left[\delta_1+\delta_2-32\lambda_8^2 w^4\right]-4\mathrm{Re}\mu_3^2\left[\delta_3-8\lambda_8 w^2\right]}\\
\theta_{15} &= \frac{2v\left(2w+\sqrt{2}\right)\epsilon\left(-8\sin(2\beta)\mathrm{Re}\mu_5^2+4\mathrm{Re}\mu_3^2+v^2\sin^3(2\beta)(\lambda_{1234})\right)}{2\mathrm{Re}\mu_3^2\left[\delta_4-16\mathrm{Re}\mu_5^2\right]+\sin(2\beta)\left[64(\mathrm{Re}\mu_5^2)^2+\delta_5+v^4\sin^2(2\beta)\left(4\lambda_1\lambda_2-(\lambda_3+\lambda_4)^2\right)\right]}\\
\theta_{23} &= \frac{\epsilon\csc(2\beta)\left(8\cot(2\beta)\mathrm{Re}\mu_3^2-v^2(4\cos(2\beta)(\lambda_1+\lambda_2)+(\cos(4\beta)+3)(\lambda_1-\lambda_2))\right)}{4\mathrm{Re}\mu_3^2(\lambda_1+\lambda_2-\lambda_3-\lambda_4)+v^2\sin(2\beta)\left((\lambda_3+\lambda_4)^2-4\lambda_1\lambda_2\right)}\\
\theta_{24} &= \frac{16v^3\left(3w+\sqrt{2}\right)\epsilon\sin^2(\beta)\cos^2(\beta)(\cos(2\beta)(\lambda_{1234})+\lambda_1-\lambda_2)}{\sin(2\beta)\left[\delta_6+\delta_7-32\lambda_8^2 w^4\right]-4\mathrm{Re}\mu_3^2\left[\delta_8-8\lambda_8 w^2\right]}\\
\theta_{25} &= -\frac{2v^3\left(2w+\sqrt{2}\right)\epsilon\sin^2(2\beta)(\cos(2\beta)(\lambda_1+\lambda_2-\lambda_3-\lambda_4)+\lambda_1-\lambda_2)}{\sin(2\beta)\left[\delta_9+v^4\sin^2(2\beta)\left((\lambda_3+\lambda_4)^2-4\lambda_1\lambda_2\right)\right]-2\mathrm{Re}\mu_3^2\left[\delta_{10}-16\mathrm{Re}(\mu_5^2)\right]}\\
\theta_{34} &= 0\\
\theta_{35} &= 0\\
\theta_{45} &= \frac{\epsilon\left(-\sqrt{2}v^2+12w^3+4\sqrt{2}w^2-2\sqrt{2}\right)}{4\lambda_8 w^3-8w\mathrm{Re}\mu_5^2},
\end{aligned}
\tag{D.4}
$$

where

$$
\begin{aligned}
\delta_1 &= v^4\left[\cos(4\beta)\left(4\lambda_1\lambda_2-(\lambda_3+\lambda_4)^2\right)-4\lambda_1\lambda_2+\lambda_3^2+2\lambda_3\lambda_4+\lambda_4^2\right]\\
\delta_2 &= v^2w^2\left[16\lambda_8\cos(2\beta)(\lambda_1-\lambda_2)+16\lambda_1\lambda_8+16\lambda_2\lambda_8\right]\\
\delta_3 &= v^2\left[\cos(4\beta)(\lambda_{1234})+4\cos(2\beta)(\lambda_1-\lambda_2)+3\lambda_1+3\lambda_2+\lambda_3+\lambda_4\right]\\
\delta_4 &= v^2\left[\cos(4\beta)(\lambda_{1234})+4\cos(2\beta)(\lambda_1-\lambda_2)+3\lambda_1+3\lambda_2+\lambda_3+\lambda_4\right]\\
\delta_5 &= -16v^2\mathrm{Re}\mu_5^2[\cos(2\beta)(\lambda_1-\lambda_2)+\lambda_1+\lambda_2]\\
\delta_6 &= v^4\left[\cos(4\beta)\left(4\lambda_1\lambda_2-(\lambda_3+\lambda_4)^2\right)-4\lambda_1\lambda_2+\lambda_3^2+2\lambda_3\lambda_4+\lambda_4^2\right]\\
\delta_7 &= v^2w^2\left[16\lambda_8\cos(2\beta)(\lambda_1-\lambda_2)+16\lambda_1\lambda_8+16\lambda_2\lambda_8\right]\\
\delta_8 &= v^2\left[\cos(4\beta)(\lambda_1+\lambda_2-\lambda_3-\lambda_4)+4\cos(2\beta)(\lambda_1-\lambda_2)+3\lambda_1+3\lambda_2+\lambda_3+\lambda_4\right]\\
\delta_9 &= -64(\mathrm{Re}\mu_5^2)^2+16v^2\mathrm{Re}\mu_5^2(\cos(2\beta)(\lambda_1-\lambda_2)+\lambda_1+\lambda_2)\\
\delta_{10} &= v^2\left[\cos(4\beta)(\lambda_{1234})+4\cos(2\beta)(\lambda_1-\lambda_2)+3\lambda_1+3\lambda_2+\lambda_3+\lambda_4\right].
\end{aligned}
$$

JHEP09(2018)059

References

[1] V.A. Kuzmin, V.A. Rubakov and M.E. Shaposhnikov, *On the Anomalous Electroweak Baryon Number Nonconservation in the Early Universe*, *Phys. Lett.* **B 155** (1985) 36 [INSPIRE].

[2] K. Kajantie, M. Laine, K. Rummukainen and M.E. Shaposhnikov, *Is there a hot electroweak phase transition at $m_H \gtrsim m_W$?*, *Phys. Rev. Lett.* **77** (1996) 2887 [hep-ph/9605288] [INSPIRE].

[3] V. Silveira and A. Zee, *Scalar phantoms*, *Phys. Lett.* **B 161** (1985) 136 [INSPIRE].

[4] J. McDonald, *Gauge singlet scalars as cold dark matter*, *Phys. Rev.* **D 50** (1994) 3637 [hep-ph/0702143] [INSPIRE].

[5] J.M. Cline and K. Kainulainen, *Electroweak baryogenesis and dark matter from a singlet Higgs*, *JCAP* **01** (2013) 012 [arXiv:1210.4196] [INSPIRE].

[6] T. Alanne, K. Kainulainen, K. Tuominen and V. Vaskonen, *Baryogenesis in the two doublet and inert singlet extension of the Standard Model*, *JCAP* **08** (2016) 057 [arXiv:1607.03303] [INSPIRE].

[7] M. Lindner, M. Platscher and F.S. Queiroz, *A Call for New Physics: The Muon Anomalous Magnetic Moment and Lepton Flavor Violation*, *Phys. Rept.* **731** (2018) 1 [arXiv:1610.06587] [INSPIRE].

[8] L. Bian and N. Chen, *Cancellation mechanism in the predictions of electric dipole moments*, *Phys. Rev.* **D 95** (2017) 115029 [arXiv:1608.07975] [INSPIRE].

[9] K. Kowalska and E.M. Sessolo, *Expectations for the muon g-2 in simplified models with dark matter*, *JHEP* **09** (2017) 112 [arXiv:1707.00753] [INSPIRE].

[10] Muon g-2 collaboration, G.W. Bennett et al., *Final Report of the Muon E821 Anomalous Magnetic Moment Measurement at BNL*, *Phys. Rev.* **D 73** (2006) 072003 [hep-ex/0602035] [INSPIRE].

[11] T. Blum et al., *The Muon (g-2) Theory Value: Present and Future*, arXiv:1311.2198 [INSPIRE].

[12] ACME collaboration, J. Baron et al., *Order of Magnitude Smaller Limit on the Electric Dipole Moment of the Electron*, *Science* **343** (2014) 269 [arXiv:1310.7534] [INSPIRE].

[13] J. McDonald, *Electroweak baryogenesis and dark matter via a gauge singlet scalar*, *Phys. Lett.* **B 323** (1994) 339 [INSPIRE].

[14] S. Profumo, M.J. Ramsey-Musolf and G. Shaughnessy, *Singlet Higgs phenomenology and the electroweak phase transition*, *JHEP* **08** (2007) 010 [arXiv:0705.2425] [INSPIRE].

[15] V. Barger, P. Langacker, M. McCaskey, M. Ramsey-Musolf and G. Shaughnessy, *Complex Singlet Extension of the Standard Model*, *Phys. Rev.* **D 79** (2009) 015018 [arXiv:0811.0393] [INSPIRE].

[16] A. Ahriche and S. Nasri, *Light Dark Matter, Light Higgs and the Electroweak Phase Transition*, *Phys. Rev.* **D 85** (2012) 093007 [arXiv:1201.4614] [INSPIRE].

[17] N. Turok and J. Zadrozny, *Electroweak baryogenesis in the two doublet model*, *Nucl. Phys.* **B 358** (1991) 471 [INSPIRE].

JHEP09(2018)059

[18] N. Turok and J. Zadrozny, *Phase transitions in the two doublet model*, *Nucl. Phys.* **B 369** (1992) 729 [INSPIRE].

[19] K. Funakubo, A. Kakuto and K. Takenaga, *The Effective potential of electroweak theory with two massless Higgs doublets at finite temperature*, *Prog. Theor. Phys.* **91** (1994) 341 [hep-ph/9310267] [INSPIRE].

[20] A.T. Davies, C.D. froggatt, G. Jenkins and R.G. Moorhouse, *Baryogenesis constraints on two Higgs doublet models*, *Phys. Lett.* **B 336** (1994) 464 [INSPIRE].

[21] J.M. Cline, K. Kainulainen and A.P. Vischer, *Dynamics of two Higgs doublet CP-violation and baryogenesis at the electroweak phase transition*, *Phys. Rev.* **D 54** (1996) 2451 [hep-ph/9506284] [INSPIRE].

[22] M. Laine and K. Rummukainen, *Two Higgs doublet dynamics at the electroweak phase transition: A Nonperturbative study*, *Nucl. Phys.* **B 597** (2001) 23 [hep-lat/0009025] [INSPIRE].

[23] L. Fromme, S.J. Huber and M. Seniuch, *Baryogenesis in the two-Higgs doublet model*, *JHEP* **11** (2006) 038 [hep-ph/0605242] [INSPIRE].

[24] P. Basler, M. Krause, M. Muhlleitner, J. Wittbrodt and A. Wlotzka, *Strong First Order Electroweak Phase Transition in the CP-Conserving 2HDM Revisited*, *JHEP* **02** (2017) 121 [arXiv:1612.04086] [INSPIRE].

[25] P. Basler, M. Mühlleitner and J. Wittbrodt, *The CP-Violating 2HDM in Light of a Strong First Order Electroweak Phase Transition and Implications for Higgs Pair Production*, *JHEP* **03** (2018) 061 [arXiv:1711.04097] [INSPIRE].

[26] C. Bonilla, D. Sokolowska, N. Darvishi, J.L. Diaz-Cruz and M. Krawczyk, *IDMS: Inert Dark Matter Model with a complex singlet*, *J. Phys.* **G 43** (2016) 065001 [arXiv:1412.8730] [INSPIRE].

[27] M. Kakizaki, A. Santa and O. Seto, *Phenomenological signatures of mixed complex scalar WIMP dark matter*, *Int. J. Mod. Phys.* **A 32** (2017) 1750038 [arXiv:1609.06555] [INSPIRE].

[28] E.J. Chun, *The muon g-2 in two-Higgs-doublet models*, *EPJ Web Conf.* **118** (2016) 01006 [arXiv:1511.05225] [INSPIRE].

[29] A. Broggio, E.J. Chun, M. Passera, K.M. Patel and S.K. Vempati, *Limiting two-Higgs-doublet models*, *JHEP* **11** (2014) 058 [arXiv:1409.3199] [INSPIRE].

[30] K.-m. Cheung, C.-H. Chou and O.C.W. Kong, *Muon anomalous magnetic moment, two Higgs doublet model and supersymmetry*, *Phys. Rev.* **D 64** (2001) 111301 [hep-ph/0103183] [INSPIRE].

[31] R. Harnik, J. Kopp and J. Zupan, *Flavor Violating Higgs Decays*, *JHEP* **03** (2013) 026 [arXiv:1209.1397] [INSPIRE].

[32] C.P. Burgess, M. Pospelov and T. ter Veldhuis, *The Minimal model of nonbaryonic dark matter: A Singlet scalar*, *Nucl. Phys.* **B 619** (2001) 709 [hep-ph/0011335] [INSPIRE].

[33] H. Davoudiasl, R. Kitano, T. Li and H. Murayama, *The New minimal standard model*, *Phys. Lett.* **B 609** (2005) 117 [hep-ph/0405097] [INSPIRE].

[34] C.E. Yaguna, *Gamma rays from the annihilation of singlet scalar dark matter*, *JCAP* **03** (2009) 003 [arXiv:0810.4267] [INSPIRE].

JHEP09(2018)059

[35] R.N. Lerner and J. McDonald, *Gauge singlet scalar as inflaton and thermal relic dark matter*, *Phys. Rev.* **D 80** (2009) 123507 [arXiv:0909.0520] [INSPIRE].

[36] ATLAS and CMS collaborations, *Measurements of the Higgs boson production and decay rates and constraints on its couplings from a combined ATLAS and CMS analysis of the LHC pp collision data at* $\sqrt{s} = 7$ *and* 8 *TeV*, ATLAS-CONF-2015-044.

[37] A. Falkowski, C. Gross and O. Lebedev, *A second Higgs from the Higgs portal*, *JHEP* **05** (2015) 057 [arXiv:1502.01361] [INSPIRE].

[38] J.R. Espinosa, B. Gripaios, T. Konstandin and F. Riva, *Electroweak Baryogenesis in Non-minimal Composite Higgs Models*, *JCAP* **01** (2012) 012 [arXiv:1110.2876] [INSPIRE].

[39] G.C. Branco, L. Lavoura and J.P. Silva, *CP Violation*, *Int. Ser. Monogr. Phys.* **103** (1999) 1 [INSPIRE].

[40] T.D. Lee, *A Theory of Spontaneous T Violation*, *Phys. Rev.* **D 8** (1973) 1226 [INSPIRE].

[41] J.F. Gunion, H.E. Haber, G.L. Kane and S. Dawson, *The Higgs Hunter's Guide*, *Front. Phys.* **80** (2000) 1 [INSPIRE].

[42] G.C. Branco, P.M. Ferreira, L. Lavoura, M.N. Rebelo, M. Sher and J.P. Silva, *Theory and phenomenology of two-Higgs-doublet models*, *Phys. Rept.* **516** (2012) 1 [arXiv:1106.0034] [INSPIRE].

[43] V. Keus, S.F. King, S. Moretti and K. Yagyu, *CP Violating Two-Higgs-Doublet Model: Constraints and LHC Predictions*, *JHEP* **04** (2016) 048 [arXiv:1510.04028] [INSPIRE].

[44] V. Zarikas, *The Phase transition of the two Higgs extension of the standard model*, *Phys. Lett.* **B 384** (1996) 180 [hep-ph/9509338] [INSPIRE].

[45] A.B. Lahanas, V.C. Spanos and V. Zarikas, *Charge asymmetry in two-Higgs doublet model*, *Phys. Lett.* **B 472** (2000) 119 [hep-ph/9812535] [INSPIRE].

[46] G. Aliferis, G. Kofinas and V. Zarikas, *Efficient electroweak baryogenesis by black holes*, *Phys. Rev.* **D 91** (2015) 045002 [arXiv:1406.6215] [INSPIRE].

[47] S.L. Glashow and S. Weinberg, *Natural Conservation Laws for Neutral Currents*, *Phys. Rev.* **D 15** (1977) 1958 [INSPIRE].

[48] E.A. Paschos, *Diagonal Neutral Currents*, *Phys. Rev.* **D 15** (1977) 1966 [INSPIRE].

[49] V.D. Barger, J.L. Hewett and R.J.N. Phillips, *New Constraints on the Charged Higgs Sector in Two Higgs Doublet Models*, *Phys. Rev.* **D 41** (1990) 3421 [INSPIRE].

[50] H.E. Haber and D. O'Neil, *Basis-independent methods for the two-Higgs-doublet model. II. The Significance of* $\tan\beta$, *Phys. Rev.* **D 74** (2006) 015018 [*Erratum ibid.* **D 74** (2006) 059905] [hep-ph/0602242] [INSPIRE].

[51] S. Davidson and H.E. Haber, *Basis-independent methods for the two-Higgs-doublet model*, *Phys. Rev.* **D 72** (2005) 035004 [*Erratum ibid.* **D 72** (2005) 099902] [hep-ph/0504050] [INSPIRE].

[52] F. Mahmoudi and O. Stal, *Flavor constraints on the two-Higgs-doublet model with general Yukawa couplings*, *Phys. Rev.* **D 81** (2010) 035016 [arXiv:0907.1791] [INSPIRE].

[53] A. Cherchiglia, P. Kneschke, D. Stöckinger and H. Stöckinger-Kim, *The muon magnetic moment in the 2HDM: complete two-loop result*, *JHEP* **01** (2017) 007 [arXiv:1607.06292] [INSPIRE].

JHEP09(2018)059

[54] T. Abe, R. Sato and K. Yagyu, *Lepton-specific two Higgs doublet model as a solution of muon g-2 anomaly*, *JHEP* **07** (2015) 064 [arXiv:1504.07059] [INSPIRE].

[55] A. Cherchiglia, D. Stöckinger and H. Stöckinger-Kim, *Muon g-2 in the 2HDM: maximum results and detailed phenomenology*, *Phys. Rev.* **D 98** (2018) 035001 [arXiv:1711.11567] [INSPIRE].

[56] V. Keus, *CP violation and BSM Higgs bosons*, PoS(CHARGED2016)017 [arXiv:1612.03629] [INSPIRE].

[57] B. Grzadkowski, O.M. Ogreid and P. Osland, *Natural Multi-Higgs Model with Dark Matter and CP-violation*, *Phys. Rev.* **D 80** (2009) 055013 [arXiv:0904.2173] [INSPIRE].

[58] S. Kanemura, T. Kubota and E. Takasugi, *Lee-Quigg-Thacker bounds for Higgs boson masses in a two doublet model*, *Phys. Lett.* **B 313** (1993) 155 [hep-ph/9303263] [INSPIRE].

[59] A.G. Akeroyd, A. Arhrib and E.-M. Naimi, *Note on tree level unitarity in the general two Higgs doublet model*, *Phys. Lett.* **B 490** (2000) 119 [hep-ph/0006035] [INSPIRE].

[60] M.E. Peskin and T. Takeuchi, *Estimation of oblique electroweak corrections*, *Phys. Rev.* **D 46** (1992) 381 [INSPIRE].

[61] H.E. Haber and D. O'Neil, *Basis-independent methods for the two-Higgs-doublet model III: The CP-conserving limit, custodial symmetry and the oblique parameters S, T, U*, *Phys. Rev.* **D 83** (2011) 055017 [arXiv:1011.6188] [INSPIRE].

[62] GFITTER GROUP collaboration, M. Baak et al., *The global electroweak fit at NNLO and prospects for the LHC and ILC*, *Eur. Phys. J.* **C 74** (2014) 3046 [arXiv:1407.3792] [INSPIRE].

[63] E.M. Dolle and S. Su, *The Inert Dark Matter*, *Phys. Rev.* **D 80** (2009) 055012 [arXiv:0906.1609] [INSPIRE].

[64] M. Misiak et al., *Updated NNLO QCD predictions for the weak radiative B-meson decays*, *Phys. Rev. Lett.* **114** (2015) 221801 [arXiv:1503.01789] [INSPIRE].

[65] C.Q. Geng and J.N. Ng, *Charged Higgs Effect in B_d^0-$\bar{B}_d^0$ Mixing, $K \to \pi\nu\bar{\nu}$ Decay and Rare Decays of B Mesons*, *Phys. Rev.* **D 38** (1988) 2857 [*Erratum ibid.* **D 41** (1990) 1715] [INSPIRE].

[66] O. Deschamps, S. Descotes-Genon, S. Monteil, V. Niess, S. T'Jampens and V. Tisserand, *The Two Higgs Doublet of Type II facing flavour physics data*, *Phys. Rev.* **D 82** (2010) 073012 [arXiv:0907.5135] [INSPIRE].

[67] HFLAV collaboration, Y. Amhis et al., *Averages of b-hadron, c-hadron and τ-lepton properties as of summer 2016*, *Eur. Phys. J.* **C 77** (2017) 895 [arXiv:1612.07233] [INSPIRE].

[68] BABAR collaboration, J.P. Lees et al., *Evidence for an excess of $\bar{B} \to D^{(*)}\tau^-\bar{\nu}_\tau$ decays*, *Phys. Rev. Lett.* **109** (2012) 101802 [arXiv:1205.5442] [INSPIRE].

[69] ATLAS collaboration, *Search for new resonances in $W\gamma$ and $Z\gamma$ final states in pp collisions at $\sqrt{s} = 8$ TeV with the ATLAS detector*, *Phys. Lett.* **B 738** (2014) 428 [arXiv:1407.8150] [INSPIRE].

[70] ATLAS collaboration, *Search for Scalar Diphoton Resonances in the Mass Range 65–600 GeV with the ATLAS Detector in pp Collision Data at $\sqrt{s} = 8$ TeV*, *Phys. Rev. Lett.* **113** (2014) 171801 [arXiv:1407.6583] [INSPIRE].

JHEP09(2018)059

[71] ATLAS collaboration, *Search for neutral Higgs bosons of the minimal supersymmetric standard model in pp collisions at $\sqrt{s} = 8$ TeV with the ATLAS detector*, *JHEP* **11** (2014) 056 [arXiv:1409.6064] [INSPIRE].

[72] ATLAS collaboration, *Search for a high-mass Higgs boson decaying to a W boson pair in pp collisions at $\sqrt{s} = 8$ TeV with the ATLAS detector*, *JHEP* **01** (2016) 032 [arXiv:1509.00389] [INSPIRE].

[73] ATLAS collaboration, *Search for an additional, heavy Higgs boson in the $H \to ZZ$ decay channel at $\sqrt{s} = 8$ TeV in pp collision data with the ATLAS detector*, *Eur. Phys. J.* **C 76** (2016) 45 [arXiv:1507.05930] [INSPIRE].

[74] ATLAS collaboration, *Search for a CP-odd Higgs boson decaying to Zh in pp collisions at $\sqrt{s} = 8$ TeV with the ATLAS detector*, *Phys. Lett.* **B 744** (2015) 163 [arXiv:1502.04478] [INSPIRE].

[75] ATLAS collaboration, *Searches for Higgs boson pair production in the $hh \to bb\tau\tau, \gamma\gamma WW^*, \gamma\gamma bb, bbbb$ channels with the ATLAS detector*, *Phys. Rev.* **D 92** (2015) 092004 [arXiv:1509.04670] [INSPIRE].

[76] ATLAS collaboration, *Search for new phenomena in the $Z(\to \ell\ell) + E_{\mathrm{T}}^{\mathrm{miss}}$ final state at $\sqrt{s} = 13$ TeV with the ATLAS detector*, ATLAS-CONF-2016-056.

[77] ATLAS collaboration, *Search for diboson resonance production in the $\ell\nu qq$ final state using pp collisions at $\sqrt{s} = 13$ TeV with the ATLAS detector at the LHC*, ATLAS-CONF-2016-062.

[78] ATLAS collaboration, *Search for scalar diphoton resonances with 15.4 fb^{-1} of data collected at $\sqrt{s} = 13$ TeV in 2015 and 2016 with the ATLAS detector*, ATLAS-CONF-2016-059.

[79] ATLAS collaboration, *Search for Minimal Supersymmetric Standard Model Higgs Bosons H/A in the $\tau\tau$ final state in up to 13.3 fb^{-1} of pp collisions at $\sqrt{s} = 13$ TeV with the ATLAS Detector*, ATLAS-CONF-2016-085.

[80] ATLAS collaboration, *Search for a high-mass Higgs boson decaying to a pair of W bosons in pp collisions at $\sqrt{s} = 13$ TeV with the ATLAS detector*, ATLAS-CONF-2016-074.

[81] ATLAS collaboration, *Search for new resonances decaying to a Z boson and a photon in 13.3 fb^{-1} of pp collisions at $\sqrt{s} = 13$ TeV with the ATLAS detector*, ATLAS-CONF-2016-044.

[82] ATLAS collaboration, *Searches for heavy ZZ and ZW resonances in the llqq and vvqq final states in pp collisions at $\sqrt{s} = 13$ TeV with the ATLAS detector*, ATLAS-CONF-2016-082.

[83] ATLAS collaboration, *Study of the Higgs boson properties and search for high-mass scalar resonances in the $H \to ZZ^* \to 4\ell$ decay channel at $\sqrt{s} = 13$ TeV with the ATLAS detector*, ATLAS-CONF-2016-079.

[84] ATLAS collaboration, *Search for Higgs boson pair production in the final state of $\gamma\gamma WW^*(\to l\nu jj)$ using 13.3 fb^{-1} of pp collision data recorded at $\sqrt{s} = 13$ TeV with the ATLAS detector*, ATLAS-CONF-2016-071.

[85] ATLAS collaboration, *Search for Higgs boson pair production in the $b\bar{b}\gamma\gamma$ final state using pp collision data at $\sqrt{s} = 13$ TeV with the ATLAS detector*, ATLAS-CONF-2016-004.

[86] ATLAS collaboration, *Search for a CP-odd Higgs boson decaying to Zh in pp collisions at $\sqrt{s} = 13$ TeV with the ATLAS detector*, ATLAS-CONF-2016-015.

JHEP09(2018)059

[87] ATLAS collaboration, *Search for pair production of Higgs bosons in the $b\bar{b}b\bar{b}$ final state using proton-proton collisions at $\sqrt{s} = 13$ TeV with the ATLAS detector*, ATLAS-CONF-2016-017.

[88] CMS collaboration, *Search for a Higgs boson in the mass range from 145 to 1000 GeV decaying to a pair of W or Z bosons*, *JHEP* **10** (2015) 144 [arXiv:1504.00936] [INSPIRE].

[89] CMS collaboration, *Search for a pseudoscalar boson decaying into a Z boson and the 125 GeV Higgs boson in $\ell^+\ell^- b\bar{b}$ final states*, *Phys. Lett.* **B 748** (2015) 221 [arXiv:1504.04710] [INSPIRE].

[90] CMS collaboration, *Searches for a heavy scalar boson H decaying to a pair of 125 GeV Higgs bosons hh or for a heavy pseudoscalar boson A decaying to Zh, in the final states with $h \to \tau\tau$*, *Phys. Lett.* **B 755** (2016) 217 [arXiv:1510.01181] [INSPIRE].

[91] CMS collaboration, *Search for neutral MSSM Higgs bosons decaying into a pair of bottom quarks*, *JHEP* **11** (2015) 071 [arXiv:1506.08329] [INSPIRE].

[92] CMS collaboration, *Search for resonant pair production of Higgs bosons decaying to two bottom quark-antiquark pairs in proton-proton collisions at 8 TeV*, *Phys. Lett.* **B 749** (2015) 560 [arXiv:1503.04114] [INSPIRE].

[93] CMS collaboration, *Search for two Higgs bosons in final states containing two photons and two bottom quarks in proton-proton collisions at 8 TeV*, *Phys. Rev.* **D 94** (2016) 052012 [arXiv:1603.06896] [INSPIRE].

[94] CMS collaboration, *Search for additional neutral Higgs bosons decaying to a pair of tau leptons in pp collisions at $\sqrt{s} = 7$ and 8 TeV*, CMS-PAS-HIG-14-029.

[95] CMS collaboration, *Search for scalar resonances in the 200–1200 GeV mass range decaying into a Z and a photon in pp collisions at $\sqrt{s} = 8$ TeV*, CMS-PAS-HIG-16-014.

[96] CMS collaboration, *Search for high-mass resonances in $\mathrm{Z}(\mathrm{q}\bar{\mathrm{q}})\gamma$ final state in pp collisions at $\sqrt{s} = 13$ TeV with 12.9 fb^{-1}*, CMS-PAS-EXO-16-035.

[97] CMS collaboration, *Search for resonant production of high mass photon pairs using 12.9 fb^{-1} of proton-proton collisions at $\sqrt{s} = 13$ TeV and combined interpretation of searches at 8 and 13 TeV*, CMS-PAS-EXO-16-027.

[98] CMS collaboration, *Measurements of properties of the Higgs boson and search for an additional resonance in the four-lepton final state at $\sqrt{s} = 13$ TeV*, CMS-PAS-HIG-16-033.

[99] CMS collaboration, *Search for high mass Higgs to WW with fully leptonic decays using 2015 data*, CMS-PAS-HIG-16-023.

[100] CMS collaboration, *Search for resonant Higgs boson pair production in the $\mathrm{b}\bar{\mathrm{b}}\tau^+\tau^-$ final state using 2016 data*, CMS-PAS-HIG-16-029.

[101] CMS collaboration, *Search for a narrow heavy decaying to bottom quark pairs in the 13 TeV data sample*, CMS-PAS-HIG-16-025.

[102] CMS collaboration, *Search for high-mass resonances in $Z\gamma \to e^+e^-\gamma/\mu^+\mu^-\gamma$ final states in proton-proton collisions at $\sqrt{s} = 13$ TeV*, CMS-PAS-EXO-16-034.

[103] CMS collaboration, *Search for resonant Higgs boson pair production in the $\mathrm{b}\bar{\mathrm{b}}\mathrm{l}\nu\mathrm{l}\nu$ final state at $\sqrt{s} = 13$ TeV*, CMS-PAS-HIG-16-011.

[104] CMS collaboration, *Search for a neutral MSSM Higgs boson decaying into $\tau\tau$ with 12.9 fb^{-1} of data at $\sqrt{s} = 13$ TeV*, CMS-PAS-HIG-16-037.

JHEP09(2018)059

[105] CMS collaboration, *Search for resonant pair production of Higgs bosons decaying to two bottom quark-antiquark pairs in proton-proton collisions at 13 TeV*, CMS-PAS-HIG-16-002.

[106] CMS collaboration, *Search for H(bb)H(gammagamma) decays at 13TeV*, CMS-PAS-HIG-16-032.

[107] CMS collaboration, *Model independent search for Higgs boson pair production in the* $\mathrm{b\bar{b}}\tau^+\tau^-$ *final state*, CMS-PAS-HIG-15-013.

[108] CMS collaboration, *Search for new diboson resonances in the dilepton + jets final state at* $\sqrt{s} = 13$ *TeV with 2016 data*, CMS-PAS-HIG-16-034.

[109] Particle Data Group collaboration, K.A. Olive et al., *Review of Particle Physics*, *Chin. Phys.* **C 38** (2014) 090001 [INSPIRE].

[110] A. Pierce and J. Thaler, *Natural Dark Matter from an Unnatural Higgs Boson and New Colored Particles at the TeV Scale*, *JHEP* **08** (2007) 026 [hep-ph/0703056] [INSPIRE].

[111] ATLAS collaboration, *Search for charged Higgs bosons decaying via* $H^\pm \to \tau^\pm\nu$ *in fully hadronic final states using pp collision data at* $\sqrt{s} = 8$ *TeV with the ATLAS detector*, *JHEP* **03** (2015) 088 [arXiv:1412.6663] [INSPIRE].

[112] CMS collaboration, *Search for a charged Higgs boson in pp collisions at* $\sqrt{s} = 8$ *TeV*, *JHEP* **11** (2015) 018 [arXiv:1508.07774] [INSPIRE].

[113] ATLAS collaboration, *Search for charged Higgs bosons in the* $H^\pm \to tb$ *decay channel in pp collisions at* $\sqrt{s} = 8$ *TeV using the ATLAS detector*, *JHEP* **03** (2016) 127 [arXiv:1512.03704] [INSPIRE].

[114] ATLAS collaboration, *Search for charged Higgs bosons in the* τ*+jets final state using* $14.7\, fb^{-1}$ *of pp collision data recorded at* $\sqrt{s} = 13$ *TeV with the ATLAS experiment*, ATLAS-CONF-2016-088.

[115] CMS collaboration, *Search for charged Higgs bosons with the* $\mathrm{H}^\pm \to \tau^\pm\nu_\tau$ *decay channel in the fully hadronic final state at* $\sqrt{s} = 13$ *TeV*, CMS-PAS-HIG-16-031.

[116] ATLAS collaboration, *Search for charged Higgs bosons in the* $H^\pm \to tb$ *decay channel in pp collisions at* $\sqrt{s} = 13$ *TeV using the ATLAS detector*, ATLAS-CONF-2016-089.

[117] ATLAS collaboration, *Search for new phenomena in* $t\bar{t}$ *final states with additional heavy-flavour jets in pp collisions at* $\sqrt{s} = 13$ *TeV with the ATLAS detector*, ATLAS-CONF-2016-104.

[118] ATLAS and CMS collaborations, *Measurements of the Higgs boson production and decay rates and constraints on its couplings from a combined ATLAS and CMS analysis of the LHC pp collision data at* $\sqrt{s} = 7$ *and* 8 *TeV*, *JHEP* **08** (2016) 045 [arXiv:1606.02266] [INSPIRE].

[119] ATLAS collaboration, *Search for Higgs boson production via weak boson fusion and decaying to* $b\bar{b}$ *in association with a high-energy photon in the ATLAS detector*, ATLAS-CONF-2016-063.

[120] ATLAS collaboration, *Search for the Standard Model Higgs boson produced in association with top quarks and decaying into* $b\bar{b}$ *in pp collisions at* $\sqrt{s} = 13$ *TeV with the ATLAS detector*, ATLAS-CONF-2016-080.

[121] ATLAS collaboration, *Combined measurements of the Higgs boson production and decay rates in* $H \to ZZ^* \to 4\ell$ *and* $H \to \gamma\gamma$ *final states using pp collision data at* $\sqrt{s} = 13$ *TeV in the ATLAS experiment*, ATLAS-CONF-2016-081.

JHEP09(2018)059

[122] ATLAS collaboration, *Search for the Standard Model Higgs boson produced in association with a vector boson and decaying to a $b\bar{b}$ pair in pp collisions at 13 TeV using the ATLAS detector*, ATLAS-CONF-2016-091.

[123] ATLAS collaboration, *Measurements of the Higgs boson production cross section via Vector Boson Fusion and associated WH production in the $WW^* \to \ell\nu\ell\nu$ decay mode with the ATLAS detector at $\sqrt{s} = 13$ TeV*, ATLAS-CONF-2016-112.

[124] CMS collaboration, *Search for the standard model Higgs boson produced through vector boson fusion and decaying to bb with proton-proton collisions at $\sqrt{s} = 13$ TeV*, CMS-PAS-HIG-16-003.

[125] CMS collaboration, *Updated measurements of Higgs boson production in the diphoton decay channel at $\sqrt{s} = 13$ TeV in pp collisions at CMS.*, CMS-PAS-HIG-16-020.

[126] CMS collaboration, *Observation of the SM scalar boson decaying to a pair of τ leptons with the CMS experiment at the LHC*, CMS-PAS-HIG-16-043.

[127] CMS collaboration, *Search for* $\mathrm{t\bar{t}H}$ *production in the* $\mathrm{H} \to \mathrm{b\bar{b}}$ *decay channel with 2016 pp collision data at* $\sqrt{s} = 13$ TeV, CMS-PAS-HIG-16-038.

[128] CMS collaboration, *Search for the associated production of a Higgs boson with a top quark pair in final states with a τ lepton at $\sqrt{s} = 13$ TeV*, CMS-PAS-HIG-17-003.

JHEP09(2018)059